



Radiotherapy is associated with a deletion signature that contributes to poor outcomes in patients with cancer

Emre Kocakavuk^{1,2,3}, Kevin J. Anderson¹, Frederick S. Varn¹, Kevin C. Johnson¹, Samirkumar B. Amin¹, Erik. P. Sulman⁴, Martijn P. Lolkema⁵, Floris P. Barthel^{1,6,7,8} and Roel G. W. Verhaak^{1,8}

Ionizing radiation causes DNA damage and is a mainstay for cancer treatment, but understanding of its genomic impact is limited. We analyzed mutational spectra following radiotherapy in 190 paired primary and recurrent gliomas from the Glioma Longitudinal Analysis Consortium and 3,693 post-treatment metastatic tumors from the Hartwig Medical Foundation. We identified radiotherapy-associated significant increases in the burden of small deletions (5–15 bp) and large deletions (20+ bp to chromosome-arm length). Small deletions were characterized by a larger span size, lacking breakpoint microhomology and were genomically more dispersed when compared to pre-existing deletions and deletions in non-irradiated tumors. Mutational signature analysis implicated classical non-homologous end-joining-mediated DNA damage repair and APOBEC mutagenesis following radiotherapy. A high radiation-associated deletion burden was associated with worse clinical outcomes, suggesting that effective repair of radiation-induced DNA damage is detrimental to patient survival. These results may be leveraged to predict sensitivity to radiation therapy in recurrent cancer.

Radiation therapy or radiotherapy (RT) is used in the clinical management of more than half of all patients with cancer^{1,2}. Ionizing radiation kills cells by inducing DNA damage such as double-strand breaks (DSBs), leading to cell death if left unrepaired or repaired in a manner that inhibits subsequent replication. DNA repair pathways are activated in response to DSBs, and these pathways include the error-free homologous recombination (HR) pathway and three error-prone pathways: classical non-homologous end joining (c-NHEJ), alternative end joining (a-EJ) and single-strand annealing (SSA)³. In contrast to HR, c-NHEJ, a-EJ and SSA require different lengths of microhomologous sequences present on exposed DNA ends. Whereas c-NHEJ requires no microhomologies, a-EJ (also called microhomology-mediated end joining) uses a length of 2–20 base pairs (bp) of microhomology and SSA uses >20 bp of (micro-)homology. These repair processes may cause changes in the post-treatment cancer genome that can be detected through sequencing. The identification of therapy-associated mutations may imply an effect of therapy on the tumor and can aid in characterization of therapy-resistance mechanisms. A well-known example of such a process is hypermutation following treatment with DNA-alkylating agents, observed across cancers⁴ and in particular following temozolomide (TMZ) chemotherapy of gliomas^{5,6}. Similarly, an increased burden of small deletions has been observed in radiation-induced malignancies⁷. Despite these advancements, the mutational footprints of palliative and curative radiation in sporadic tumors are not well understood.

To address this gap in knowledge, we analyzed pre- and post-treatment datasets from the Glioma Longitudinal Analysis (GLASS) cohort as well as post-treatment metastatic tumor datasets from the Hartwig Medical Foundation (HMF)^{5,8,9}. We identified a significant increase of small (5–15-bp) deletions, large (>20 bp) deletions and inversions in response to ionizing radiation, which we genomically characterized. Finally, we observed that the identified signatures were associated with worse clinical outcomes.

Results

RT drives small-deletion burden. RT and TMZ are the post-surgical standard of care for patients with glioma¹⁰. We assessed the impact of RT and/or TMZ on the somatic mutation burden, including somatic single-nucleotide variants (sSNVs) and small insertions/deletions (indels, length of 1–20 bp), in matched pre- and post-treatment glioma samples ($n=190$ patients). Of the patients from which these samples were obtained, 119 (63%) received RT and TMZ, 19 (10%) received RT alone, 13 (7%) received only TMZ, and 16 (8%) received neither RT nor TMZ. For 23/190 (12%) cases, TMZ annotation was lacking with 18 of these having received RT. For each patient, we separated mutations into pre- (present in the primary tumor) and post-treatment (acquired, present only in the recurrent tumor). We then calculated the mutation burden (average mutation frequency per megabase) of post-treatment mutations. A median of 0.68 new small deletions per megabase was acquired in recurrent RT-treated (RT⁺) glioma, which was significantly higher than the median of 0.19 new small deletions per megabase acquired

¹The Jackson Laboratory for Genomic Medicine, Farmington, CT, USA. ²DKFZ Division of Translational Neurooncology at the West German Cancer Center, German Cancer Consortium Partner Site, University Hospital Essen, Essen, Germany. ³Department of Neurosurgery, University Hospital Essen, Essen, Germany. ⁴NYU Langone Health, New York, NY, USA. ⁵Department of Medical Oncology, Erasmus MC Cancer Institute, Rotterdam, the Netherlands. ⁶Department of Pathology, Brain Tumor Center Amsterdam, Amsterdam UMC, Vrije Universiteit Amsterdam, Amsterdam, the Netherlands. ⁷Present address: Cancer and Cell Biology Division, The Translational Genomics Research Institute, Phoenix, AZ, USA. ⁸These authors jointly supervised this work: Floris P. Barthel, Roel G. W. Verhaak. ✉e-mail: fbarthel@tgen.org; roel.verhaak@jax.org

in recurrent RT-naive (RT⁻) gliomas (Fig. 1a, $P=5.1 \times 10^{-3}$, Mann–Whitney *U* test), and significantly higher than the small-deletion burden detected at diagnosis (Fig. 1b). RT was not associated with a significant increase in sSNV burden (Extended Data Fig. 1a, $P=4.7 \times 10^{-1}$, Mann–Whitney *U* test) or small-insertion burden (Extended Data Fig. 1a, $P=6.7 \times 10^{-1}$, Mann–Whitney *U* test). The small-deletion increase was particularly pronounced in gliomas marked by the presence of mutations in *IDH1*, a clinically relevant subtype¹¹ predominantly consisting of grade 2 and 3 gliomas (Extended Data Fig. 1b, $P=1.4 \times 10^{-2}$, Mann–Whitney *U* test). The number of RT⁻ recurrent cases among *IDH*-wild-type glioma was too small to test for differences ($n=2$, versus $n=107$ RT-treated cases). To ensure that these changes were not due to TMZ-associated hypermutation (>10 mutations per megabase at recurrence)⁵, we stratified the cohort by hypermutation status. Hypermutation associated with small-deletion increase independent of RT treatment, whereas among non-hypermutators only RT⁺ patients showed a significant increase in small deletions (Fig. 1b, $P=5.0 \times 10^{-11}$, paired Wilcoxon signed-rank test). To evaluate the independence of this finding from potential confounders, we fitted a multivariable log-linear regression model that included TMZ treatment, glioma molecular subtype, time interval between surgeries and hypermutation. RT was independently associated with an increase in small deletions (Fig. 1c, $P=3 \times 10^{-3}$, *t*-test), directly attributing the observed small-deletion increase to RT treatment. Acquired small deletions were not more clonal/subclonal (Extended Data Fig. 1c, hypermutant: $P=9.3 \times 10^{-1}$, non-hypermutant: $P=8.7 \times 10^{-1}$, Mann–Whitney *U* test). Comparing the pre-treatment mutation burden and aneuploidy scores between tumors with a high and low post-treatment deletion burden revealed no significant differences, suggesting that these pre-RT tumor genomic characteristics are not predictive of RT-induced small-deletion acquisition.

Importantly, 30% (41/136) of non-hypermutant samples gained >1 deletion per megabase following RT, compared to 7% (2/27) of RT-naive non-hypermutators ($P=1.6 \times 10^{-2}$, Fisher's exact test). The association between RT treatment and mutational burden was significant for small deletions but not for insertions and sSNVs. Conversely, TMZ-associated hypermutation was correlated with a significant increase in the burden of all types of mutations (Extended Data Fig. 1d).

Following these observations, we hypothesized that RT may have similar effects in other tumor types. We evaluated whole-genome sequencing-derived mutational profiles from 3,693 metastatic tumors with complete treatment annotation (Extended Data Fig. 1e), available via the HMF⁸. We separated tumors by site of origin and compared the small-deletion burden between RT⁺ and RT⁻ tumors (Fig. 1d). RT⁺ tumors were further stratified depending on whether the treatment intent was curative (RT^{+cur}, $n=739$) or palliative (RT^{+pal}, $n=689$), which differ in cumulative radiation dosage¹². While this analysis was restricted to single-time-point mutational profiles, we observed a significantly higher small-deletion burden in RT⁺ patients across multiple tumor types, including bone/soft tissue (RT^{+cur}: median 0.15 deletions per megabase, RT⁻: median 0.08 deletions per megabase, $P=6.2 \times 10^{-4}$, Kruskal–Wallis test),

lung (RT^{+cur}: median 0.56 deletions per megabase, RT⁻: median 0.43 deletions per megabase, $P=3.4 \times 10^{-3}$, Kruskal–Wallis test) and breast (RT^{+cur}: median 0.18 deletions per megabase, RT⁻: median 0.12 deletions per megabase, $P=1.2 \times 10^{-4}$, Kruskal–Wallis test) cancers (Fig. 1d). The observed patterns were present in both non-small-cell and small-cell lung cancer but were restricted to estrogen-receptor-positive breast cancer subtypes (Extended Data Fig. 1f). Tumors receiving palliative RT frequently presented an intermediate state in between the RT⁻ and RT^{+cur} cohorts, suggesting an association between acquired small-deletion burden and RT dose.

DNA repair deficiency associates with increased mutational load⁴. We compared the small-deletion burden between HMF tumors with and without microsatellite instability (MSI) or HR deficiency (HRD)¹³. Notably, HRD⁺ and particularly MSI⁺ tumors harbored significantly more small deletions compared to HRD⁻/MSI⁻ samples (Extended Data Fig. 1g, $P<2.2 \times 10^{-16}$, Kruskal–Wallis test). RT treatment was associated with an increase in small-deletion burden in HRD⁻/MSI⁻ (Extended Data Fig. 1g, $P=6.0 \times 10^{-8}$, Mann–Whitney *U* test) and HRD⁺ ($P=3.5 \times 10^{-2}$) tumors, but not in MSI⁺ tumors ($P=7.1 \times 10^{-1}$). To account for the possibility that HRD and MSI confounded the association between RT treatment and the small-deletion burden, we have included HRD and MSI status in a multivariable log-linear regression analysis and found that the association between RT treatment and small-deletion burden is independent of HRD/MSI status (Extended Data Fig. 1h).

Next, we assessed whether the small-deletion burden was associated with mutations in selected genes (*ATM*, *ATR*, *CHEK1*, *CHEK2*, *PARP1*, *PRKDC*, *TP53* and *WEE1*) involved in the DNA damage response (DDR). This analysis indicated that DDR mutations in these genes were universally associated with a significantly higher small-deletion burden. We used log-linear regression to adjust for potential confounding variables, including age, tumor type, DNA damage repair background, DRR gene mutations and various cytotoxic treatment regimens (for example, taxane, platinum, anthracyclines and alkylating agents) that have previously been associated with increased mutation burdens¹⁴. Results from this analysis confirmed a robust association with an increased small-deletion burden for both palliative and curative RT (Extended Data Fig. 1h, RT^{+cur} versus RT-naive: odds ratio = 1.25, $P<1 \times 10^{-3}$, *t*-test).

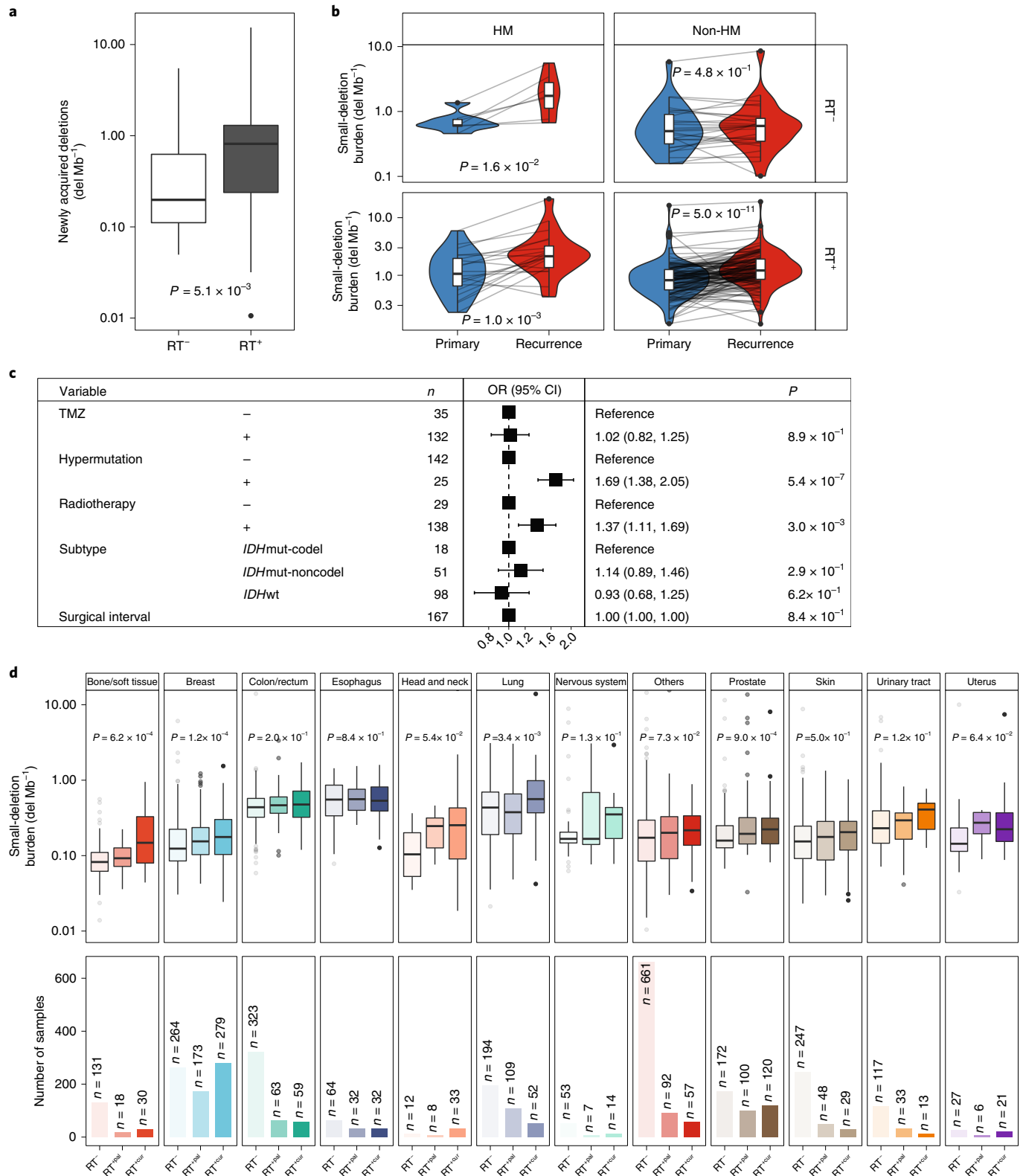
To verify the causal association between RT and acquired small deletions, we reanalyzed whole-genome sequencing data from 324 human induced pluripotent stem cells (iPSCs) exposed to various carcinogens, including two iPSCs treated with ionizing radiation¹⁵. Small-deletion burden was significantly higher in the RT⁺ iPSCs compared to controls (Extended Data Fig. 1i, $P=2.0 \times 10^{-2}$, Mann–Whitney *U* test). In contrast, there was no significant difference in small-insertion burden ($P=1.8 \times 10^{-1}$). Strikingly, the ionizing radiation group showed the highest median burden of small deletions across all treatment modalities, further substantiating our results (Extended Data Fig. 1k).

RT-associated deletions harbor a specific genomic signature. Characteristics of RT-associated small deletions, such as length

Fig. 1 | RT is associated with an increased small-deletion burden. **a**, A boxplot (in this and all following figures: boxes span quartiles, center lines represent medians, and whiskers represent absolute range, excluding outliers) depicting the burden of newly acquired/post-treatment small deletions (deletions per megabase (del Mb⁻¹)) in RT⁻ ($n=34$) and RT⁺ ($n=156$) patients from the GLASS cohort. A two-sided Mann–Whitney *U* test was applied for statistical testing. **b**, Longitudinal comparison of small-deletion burden between primary and recurrent glioma samples, separated by hypermutation (HM) and RT. A two-sided paired Wilcoxon signed-rank test was applied for statistical testing. **c**, A forest plot showing a multivariable log-linear regression model of newly acquired small-deletion burden (deletions per megabase) including TMZ treatment, hypermutation, RT treatment, molecular subtype and surgical interval (in months) as variables. A two-sided *t*-test was applied. OR, odds ratio. **d**, Top: for the metastatic cohort, boxplots depicting small-deletion burden (deletions per megabase) in RT⁻ tumor samples (left), tumor samples treated with RT with palliative intent (RT^{+pal}, middle) and tumor samples treated with RT with curative intent (RT^{+cur}, right), separated by primary tumor location. A two-sided Kruskal–Wallis test was applied for statistical testing. Bottom: sample sizes of the metastatic cohort separated by primary tumor location.

distribution and breakpoint microhomology, may provide insights into their etiology. We explored such features in GLASS *IDH*-mutant gliomas (RT⁺, *n* = 49; RT⁻, *n* = 32) as only two GLASS *IDH*-wild-type gliomas were not RT treated (versus 107 RT treated). Small deletions in RT⁺ recurrent tumor samples showed increased deletion lengths (Fig. 2a, left; RT⁺, *P* = 1.5 × 10⁻⁴; RT⁻,

P = 3.5 × 10⁻¹; paired Wilcoxon signed-rank test), which was even more pronounced in acquired deletions (Extended Data Fig. 2a, *P* = 1.3 × 10⁻⁴, Mann–Whitney *U* test), supporting the idea that RT results in longer deletions (Fig. 2a, left). Moreover, the size distribution of RT-associated deletions shifted towards deletions of length ~5–15 bp (Fig. 2a, right).



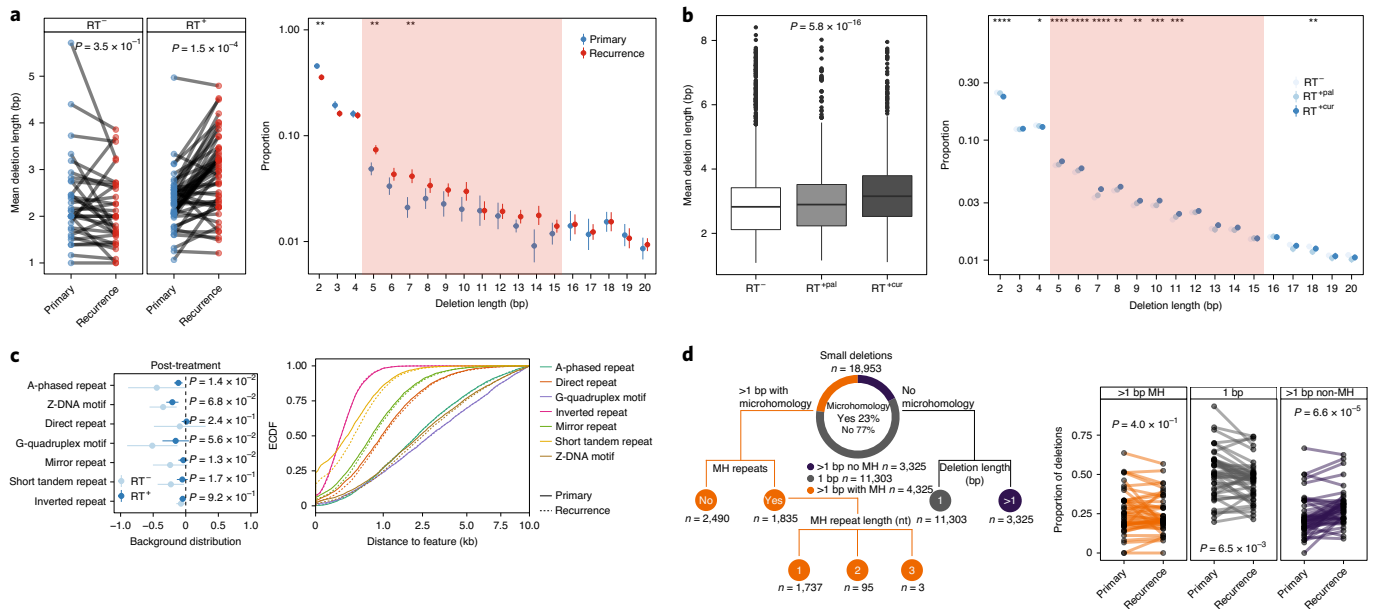


Fig. 2 | RT-associated small deletions harbor a characteristic genomic signature. **a**, Length distribution in GLASS. Left: mean deletion lengths in primary versus recurrent *IDH*-mutant glioma ($n = 81$), separated by RT treatment (RT^+ , $n = 32$, RT^- , $n = 49$). The P values were calculated using a two-sided paired Wilcoxon signed-rank test. Right: y axis, proportion of deletions; x axis, deletion length >1 bp. Proportions were calculated for each patient, with the mean (point) and 95% CI (line range) compared longitudinally in RT^+ non-hypermutable glioma ($n = 44$). $**P < 0.01$; two-sided paired Wilcoxon signed-rank test. Shaded area (5–15 bp): size range for which the most apparent differences were observed. **b**, Length distribution in HMF. Left: comparison of mean deletion lengths in RT^- versus RT^{+pal} versus RT^{+cur} samples. The P values were calculated using a two-sided Kruskal–Wallis test. Right: y axis, proportion of deletions; x axis, deletion length >1 bp. Proportions were calculated for each patient, with the mean (point) and 95% CI (line range) compared between RT^- versus RT^{+pal} versus RT^{+cur} samples. $*P < 0.05$, $**P < 0.01$, $***P < 0.001$, $****P < 0.0001$; two-sided Kruskal–Wallis test. **c**, Relation to genomic features in GLASS. Left: distribution of deletions in relation to genomic features. y axis: non-B-DNA genomic feature; x axis: \log_{10} ratio of mean distance of non-radiation-associated and radiation-associated post-treatment deletions to genomic feature over background distribution in non-hypermutable glioma samples ($n = 69$). Distribution of radiation-associated deletions shows little variability (narrow 95% CI) and resembles background distribution more closely (closer to 0). The P values were calculated using a two-sided Mann–Whitney U test. Right: empirical cumulative distribution function (ECDF, y axis) of distance to non-B-DNA features in kilobases (x axis) in post-irradiated non-hypermutable recurrent samples ($n = 44$). Neither in hypermutable, nor in RT^- non-hypermutable gliomas were longitudinal differences observed (Extended Data Fig. 2c). **d**, Small-deletion categories in GLASS. Left: separation of small deletions in the GLASS cohort into 3 major categories: 1bp (gray), >1 bp without microhomology (MH; purple) and >1 bp with microhomology (orange) in *IDH*-mutant gliomas ($n = 81$). The microhomology category was further classified based on the occurrence of microhomology repeat sequences and length of repeats. nt, nucleotide. Right: a comparison of the proportion of deletions for each RT^+ non-hypermutable glioma sample ($n = 44$, further comparisons in Extended Data Fig. 2e) using a two-sided paired Wilcoxon signed-rank test.

Comparing RT^+ and RT^- metastatic tumor samples from the single-time-point HMF dataset confirmed larger deletions in palliative and curative RT-treated tumors (Fig. 2b and Extended Data Fig. 2b), and a shift in deletion span from 1–4 bp towards 5–15 bp deletions (Fig. 2b). Deletion length was larger following curative compared to palliative RT treatment, further substantiating a dose and exposure association. Taken together, these findings suggest that RT drives a burden of small deletions with distinct characteristics.

B-DNA is the common right-handed, double-helical formation of DNA. Non-canonical non-B-DNA structures and fragile repeat-rich DNA may be more prone to acquiring mutations¹⁶, which may include RT-induced deletions. We compared the distribution of small deletions across these genomic features against a random background distribution. In the *IDH*-mutant GLASS cohort, deletions following RT showed less variability and higher similarity to the random background distribution compared to non-RT-induced deletions, and larger distances to non-B-DNA features (Fig. 2c, right, and Extended Data Fig. 2c). The lack of or reduced association between RT-associated deletions and the analyzed genomic features, such as repeats and G-quadruplex motifs, suggests that RT-associated small deletions occur in a stochastic manner, independent of the intrinsic mutagenicity of the fragile genome regions analyzed.

We assessed whether RT-associated small deletions showed enrichment in driver genes. We computed the covariate-adjusted normalized ratio between non-synonymous and synonymous mutations (dN/dS), to identify selection of mutations at the level of individual genes and separately for GLASS pre- and post-treatment fractions (Extended Data Fig. 2d)¹⁷. We did not find evidence for significant selection for any genes in the post-treatment fraction following RT. In the HMF set, where pre-treatment samples are unavailable, we could not perform this analysis. Our results in *IDH*-mutant glioma further support the notion that RT-associated deletions do not occur at particular genomic loci.

Small deletions can be the result of error-prone DSB repair mechanisms such as c-NHEJ and a-EJ³. We characterized deletions on the basis of size, microhomology and repeat content to investigate which mechanism is used for DSB repair following RT (Fig. 2d and Extended Data Fig. 2e). Deletions without microhomology comprised the majority of deletions in the dataset (77%, Fig. 2d). However, in non-hypermutable gliomas receiving ionizing radiation, we observed a significant increase in >1 -bp deletions without microhomology (Fig. 2d, $P = 6.6 \times 10^{-5}$, paired Wilcoxon signed-rank test) and conversely a decrease in 1-bp deletions (Fig. 2d, $P = 6.5 \times 10^{-3}$, paired Wilcoxon signed-rank test). Comparison of RT^+ and RT^- metastatic tumors from the HMF dataset demonstrated comparable

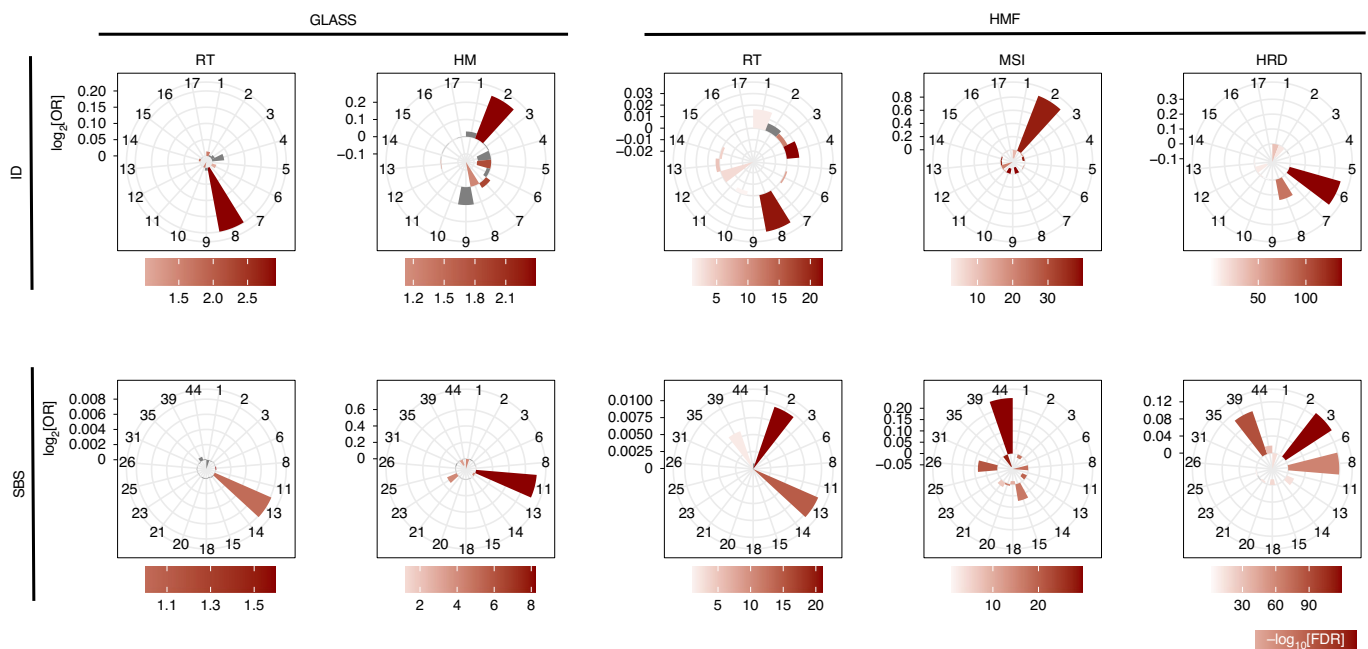


Fig. 3 | ID8 and APOBEC SBS signatures associated with RT. Indel (ID) and SBS mutational signatures in the GLASS and HMF cohorts associated with RT, hypermutation, MSI and HRD. RT⁺ mean contribution = 0.22 versus RT⁻ mean contribution = 0.07, $P = 7.4 \times 10^{-5}$, $Q = 3.8 \times 10^{-3}$, two-sided Mann-Whitney U test and FDR, respectively. Bars in the petal plots not reaching statistical significance (defined as $FDR < 0.01$) are indicated in gray.

results (Extended Data Fig. 2f). These data suggest that c-NHEJ is the preferred pathway for repairing radiation-induced DNA damage.

Distinct mutational signatures associated with RT. Cancer cells accumulate somatic mutations through mechanisms that may leave distinct genomic scars, termed mutational signatures¹⁸. To determine the mutational processes of RT, we compared pre- and post-treatment mutations in the GLASS dataset to previously defined mutational signatures¹⁸. The comparison of signature contributions between post-recurrence mutations in RT⁺ and RT⁻ *IDH*-mutant glioma samples revealed a strong enrichment of indel signature 8 (ID8; Fig. 3 and Extended Data Fig. 3d; RT⁺ mean contribution = 0.22 versus RT⁻ mean contribution = 0.07, $P = 7.4 \times 10^{-5}$, $Q = 3.8 \times 10^{-3}$, Mann-Whitney U test and false discovery rate (FDR), respectively). In RT⁺ but not RT⁻ patients, comparing ID8 values before and after treatment revealed significant increases in absolute (Extended Data Fig. 3e, $P = 4.5 \times 10^{-7}$, paired Wilcoxon rank-signed test) and relative (Extended Data Fig. 3e, $P = 2.3 \times 10^{-3}$) ID8 contributions, post-treatment. ID8 is composed of ≥ 5 -bp deletions without microhomology and has previously been linked to DSB repair by c-NHEJ, suggesting radiation-induced DSB repair via c-NHEJ¹⁸. As expected, hypermutation due to TMZ treatment in *IDH*-mutant gliomas was associated with ID2, which is reported to be elevated in mismatch-repair-deficient tumors (Fig. 3 and Extended Data Fig. 3a,b)¹⁸.

A previous mutational signature analysis in the HMF dataset observed the strongest association between RT and ID6¹⁴. Confirming our findings in the GLASS cohort, we observed the strongest association with ID8 in the HMF dataset, and significant but less pronounced association for ID6 (Fig. 3). Both absolute and relative ID8 values were significantly higher in RT⁺ samples when compared to RT⁻ samples, and a significant association was observed in nine of twelve tumor types (Extended Data Fig. 3f). The comparison of HRD⁺ and HRD⁻ samples associated HRD with ID6. ID6 comprises >5 -bp deletions with microhomology at breakpoints and

is elevated in HRD⁺ breast cancers¹⁹. Analogous to TMZ-associated hypermutators in GLASS, MSI samples in HMF were enriched for ID2 (Fig. 3).

To summarize, while MSI leads to an increased small-deletion burden due to hypermutability from impaired DNA mismatch repair at microsatellites/homopolymers, DSBs due to HRD and RT are repaired via error-prone DSB repair mechanisms. Our results implicate the a-EJ pathway that utilizes microhomologies at break-points in HRD⁺ samples (signature ID6) and the c-NHEJ pathway which does not require breakpoint microhomology in RT⁺ samples (signature ID8).

We sought to identify single-base-substitution (SBS) signature associations in both datasets. We confirmed an enrichment of SBS11 in hypermutant *IDH*-mutant glioma samples^{5,20}, an enrichment of signatures SBS44, SBS26, SBS21, SBS20 and SBS15 in MSI⁺ samples¹⁸ and enrichment of SBS3 and SBS8 in HRD⁺ cases^{18,19,21} along with a previously undescribed enrichment of SBS39 (Fig. 3). In addition, in the GLASS cohort, RT treatment was significantly associated with SBS13, and in the HMF cohort, it was significantly associated with SBS2 and SBS13. SBS2 and SBS13 are APOBEC signatures^{18,22}. APOBEC cytosine deaminases are involved in retrovirus and retrotransposon restriction, and the enrichment of APOBEC signatures in RT⁺ samples in both datasets implicated APOBEC-mediated mutagenesis in RT-associated DSB repair^{23–25}. Our results support the hypothesis that mutational signatures are shaped by cycles of DNA damage and DNA repair²⁶. While RT causes DSBs that are repaired via c-NHEJ resulting in specific small deletions (ID8), APOBEC cytosine deaminases may be activated during the repair process leading to SBS2 and/or SBS13.

RT associates with aneuploidy and larger deletions. We evaluated whether RT could be associated with other types of genomic variants. We detected large structural variants, including large deletions, duplications, inversions and translocations, in the longitudinal GLASS cohort. We observed an increase in large deletions (length > 20 bp to chromosome-arm length) post-therapy in RT⁺

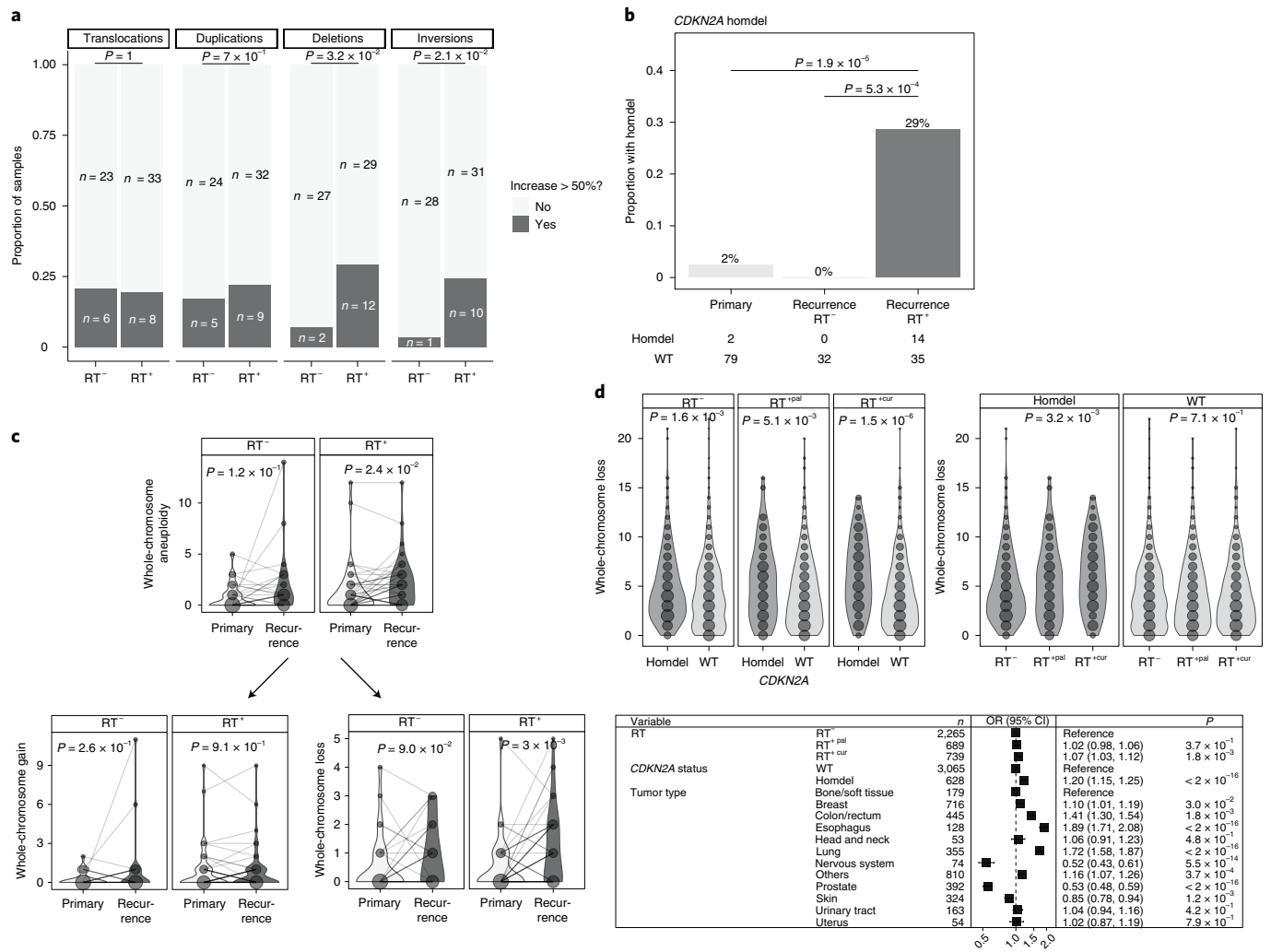


Fig. 4 | RT is associated with aneuploidy and larger deletions. **a**, RT-associated increase in large deletions and inversions. The plot shows results of an analysis of structural variants after RT in *IDH*-mutant glioma samples with sufficient quality for calling ($n = 70$): translocations, duplications, deletions and inversions. For each patient, the number of structural variants was calculated pre- and post-treatment. Based on the distribution of percentage increase from primary to recurrence, a cutoff was set for >50% increase (Extended Data Fig. 4a). Shown is a comparison of the proportion of samples with/without an increase of given structural variants between RT⁺ versus RT⁻. The *P* values were calculated using a two-sided Fisher's exact test. **b**, RT-associated *CDKN2A* homozygous deletions (homdel). Depicted are proportions of *IDH*-mutant glioma samples ($n = 81$) harboring a homozygous deletion in *CDKN2A*. Using a two-sided Fisher's exact test, proportions were compared between RT-received recurrence (RT⁺) versus RT-naive recurrence (RT⁻) versus samples before treatment (primary). Detailed distributions of whole-chromosome deletion scores are provided in Extended Data Fig. 4f. wt, wild type. **c**, RT-associated whole-chromosome aneuploidy. Upper: longitudinal comparison of whole-chromosome aneuploidy scores separated by RT treatment for *IDH*-mutant glioma samples with sufficient quality for calling and complete treatment annotation (total $n = 69$, RT⁺ $n = 42$, RT⁻ $n = 27$). Bottom: separation of whole-chromosome aneuploidy into whole-chromosome gain (left) and whole-chromosome loss (right) scores, respectively. The size of the dots is proportional to the frequency of whole-chromosome loss integers for each subgroup. The *P* values were calculated using a two-sided paired Wilcoxon rank-sum test. **d**, Validation of structural variant and aneuploidy results in HMF. Upper: comparison of whole-chromosome deletion scores between RT⁻ versus RT^{+pal} versus RT^{+cur} and/or *CDKN2A* homozygous deletion versus wild-type samples. Note that *CDKN2A* homozygous deletion is associated with higher whole-chromosome deletion scores, independent of RT. Within samples with *CDKN2A* homozygous deletion, samples that were RT treated with curative intent show the highest deletion scores. The size of the dots is proportional to the frequency of whole-chromosome loss integers for each subgroup. The *P* values were calculated using a two-sided Kruskal-Wallis test. Detailed distributions of whole-chromosome deletion scores are provided in Extended Data Fig. 4g. Bottom: a multivariable Poisson regression model for whole-chromosome deletion scores integrating RT, *CDKN2A* and tumor type as variables. A two-sided Wald test was applied.

patients, compared to RT⁻ patients (Fig. 4a, $P = 3.2 \times 10^{-2}$, Fisher's exact test). We also found a statistically significant increase in inversions (Fig. 4a, $P = 2.1 \times 10^{-2}$) and no differences in translocations (Fig. 4a, $P = 1$) and duplications (Fig. 4a, $P = 7 \times 10^{-1}$). These associations remained significant after accounting for potentially confounding factors such as TMZ treatment and molecular subtype

(Extended Data Fig. 4b). While radiation-induced secondary malignancies were reported to contain increased rates of inversions⁷, a concomitant increase in large deletions in association with RT has not previously been observed.

We next evaluated whether deletions at specific loci were associated with RT. In the *IDH*-mutant GLASS cohort, where *CDKN2A*

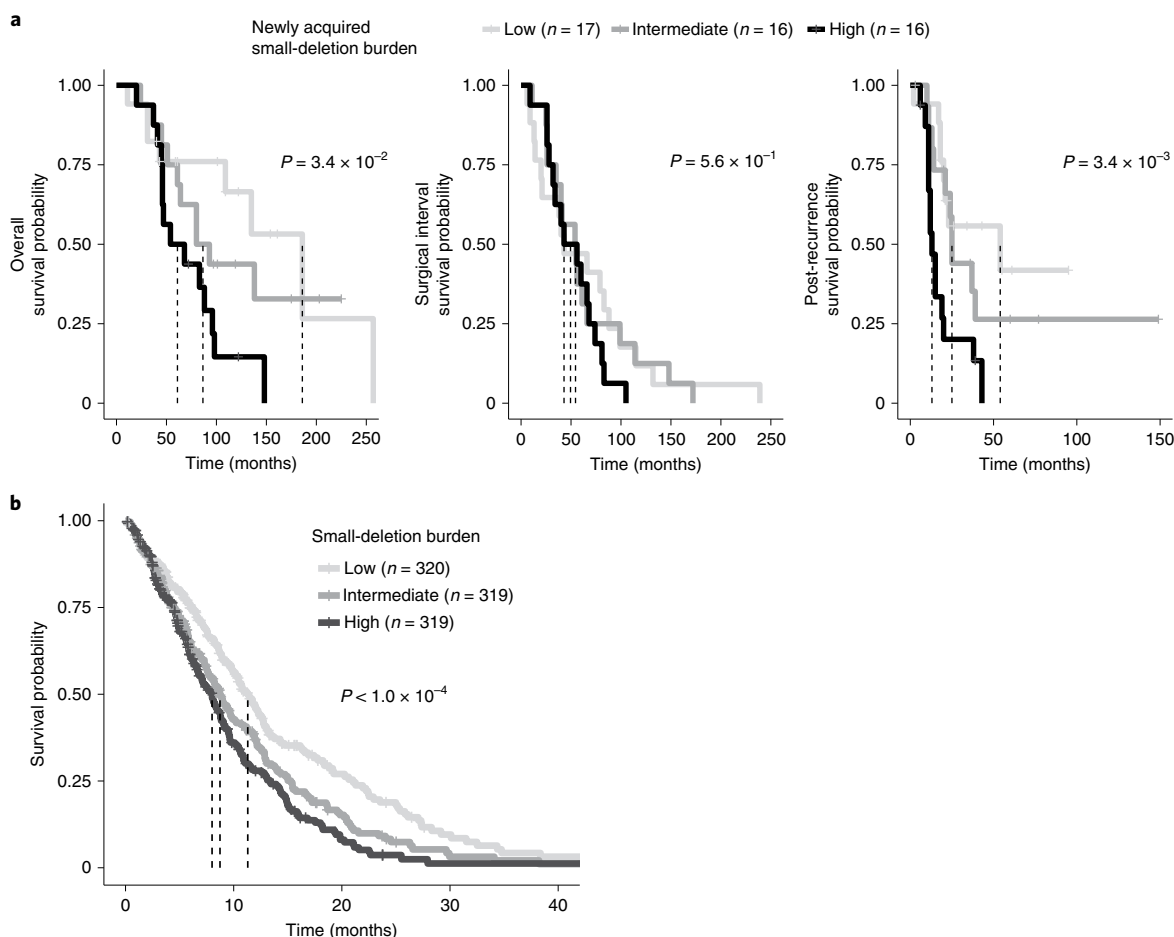


Fig. 5 | RT-associated genomic changes are linked to poor survival. a, Association of RT-related deletions with survival in GLASS. Left: Kaplan-Meier survival plots comparing overall survival dependent on deletion burden at recurrence using a log-rank test in RT⁺ *IDH*-mutant glioma samples ($n = 49$ with available survival information). Samples were separated into 3 tertiles based on deletion burden at recurrence: high (top tertile), intermediate (middle tertile) and low (bottom tertile). Dotted lines indicate median overall survival times. Note the stepwise association of tertiles with survival. Middle: Kaplan-Meier survival plots comparing surgical interval/time to second surgery dependent on deletion burden at recurrence using a two-sided log-rank test. Right: Kaplan-Meier survival plots comparing post-recurrence survival dependent on deletion burden at recurrence using a two-sided log-rank test. **b**, Association of RT-related deletions with survival in HMF. Shown are Kaplan-Meier survival plots comparing survival time dependent on deletion burden at metastasis using a two-sided log-rank test in RT⁺ metastases ($n = 958$ with available survival information). Samples were separated into 3 tertiles based on deletion burden: high (top tertile), intermediate (middle tertile) and low (bottom tertile). Dotted lines indicate median survival times. Note the stepwise association of tertiles with survival.

loss at initial diagnosis is rare, acquired *CDKN2A* homozygous deletions occurred exclusively in RT⁺ recurrences (Fig. 4b, 29% versus 0%, $P = 5.3 \times 10^{-4}$, Fisher's exact test)²⁷. This result nominated acquired *CDKN2A* homozygous loss as a potential biomarker for RT resistance among recurrent *IDH*-mutant gliomas, but not in *IDH*-wild-type gliomas where *CDKN2A* homozygous deletion at diagnosis is common.

Ionizing radiation can promote mitotic chromosome segregation errors through non-disjunction events causing aneuploidy^{28–31}. We investigated the association between RT and aneuploidy, separating aneuploidy events into gains or losses of entire chromosomes, likely the result of segregation errors; and partial gains or losses, requiring additional DSBs (see Methods, Extended Data Fig. 4c). In the *IDH*-mutant GLASS cohort, we observed a significant association between RT and chromosome losses, but not for simple gains or complex events (Fig. 4c and Extended Data Fig. 4d), which was no longer significant after adjusting for covariates in a multivariable Poisson regression. Instead, this analysis highlighted a significant association between chromosome losses and *CDKN2A* deletions

(Extended Data Fig. 4e), implying that the increase in chromosome loss frequency following RT is specific to RT-associated acquired *CDKN2A* deletions. Using the HMF metastatic tumor cohort, we confirmed the association between *CDKN2A* homozygous deletions and chromosome losses (Fig. 4d and Extended Data Fig. 4f). In fact, both curative RT treatment and *CDKN2A* homozygous deletions were independently associated with increased number of chromosomal losses in the HMF datasets (Fig. 4d and Extended Data Fig. 4f). However, testing for interactions between *CDKN2A* deletions and RT treatment indicated a trend towards interaction between palliative/curative RT and *CDKN2A* deletions (Supplementary Table 1, $P = 9.75 \times 10^{-2}$ and $P = 4.92 \times 10^{-2}$, respectively, *t*-test). In summary, aneuploidy may not be directly associated with RT but through interactions with *CDKN2A* deletions, requiring further investigation.

RT-associated genomic changes are linked to poor survival. Finally, we wanted to ascertain whether the genomic effects of RT were relevant to patient outcomes. As expected, *CDKN2A*

homozygous deletion at recurrence was significantly associated with worse overall survival in *IDH*-mutant glioma samples (Extended Data Fig. 5a, $P < 1 \times 10^{-4}$, log-rank test)⁵. To test for a survival association of *CDKN2A* deletions among RT⁺ patients in the HMF dataset, we selected 958 samples that received RT and had sufficient survival information available from 11 tumor types (Extended Data Fig. 1e). Patients whose tumors harbored a *CDKN2A* homozygous deletion showed worse outcomes compared to patients with *CDKN2A*-wild-type tumors (Extended Data Fig. 5b, left). Stratification of the cohort into tertiles based on genome-wide aneuploidy frequency demonstrated that low aneuploidy was linked to favorable outcomes and high aneuploidy was linked to poor outcomes (Extended Data Fig. 5b, middle). These results nominate acquired *CDKN2A* homozygous deletion as a biomarker of RT resistance after recurrence and support the clinical reassessment of *CDKN2A* status at recurrence for optimizing treatment strategies.

Independent of the poor prognostic implications of acquired *CDKN2A* deletions, GLASS patients with tumors carrying a high small-deletion burden at recurrence (top tertile) had significantly shorter overall survival (Fig. 5a, $P = 3.4 \times 10^{-2}$, log-rank test). The association remained significant when accounting for the small-deletion burden as a continuous variable and possible confounding variables, indicating a robust correlation (Extended Data Fig. 5c, HR = 1.19 (95% confidence interval (CI): 1.01–1.14); $P = 4.3 \times 10^{-2}$, Wald test). Multivariable modeling using a limited subset of patients with detailed dosage information in the GLASS cohort ($n = 21$) showed that the association between small-deletion burden and survival is dose independent ($P = 2 \times 10^{-2}$). Separating the overall survival time into surgical interval and post-recurrence survival indicated that the association of high newly acquired small-deletion burden with worse survival was limited to post-recurrence survival (Fig. 5a, $P = 3.4 \times 10^{-3}$, log-rank test). Surgical interval times did not differ significantly between the three tertiles (Fig. 5a, $P = 5.6 \times 10^{-1}$), suggesting that patients with glioma may initially benefit equally from RT, but after exposure to RT and acquisition of the deletion signature, tumors may lose sensitivity to further RT. This pattern is reminiscent of the association between hypermutant glioma and TMZ therapy²⁰.

In 958 RT⁺ samples from the HMF cohort (Extended Data Fig. 1g), we also found that patients harboring a high small-deletion burden (top tertile) had significantly shorter survival than other RT-treated patients (Fig. 5b, $P < 4 \times 10^{-4}$, log-rank test). Similarly, stratifying HMF patients into tertiles by ID8 burden associated an intermediate or high ID8 burden with poor survival and a low ID8 burden with more favorable outcomes (Extended Data Fig. 5b). Therefore, the presence of a high number of RT-associated small deletions identifies a tumor that has initially responded to therapy, but which may have lost some or all of the treatment sensitivity. Combined, these results suggest that a higher deletion burden may reflect a scenario that is favorable to the tumor characterized by proficient DNA repair resulting in less tumor cell killing and decreased treatment efficacy.

Discussion

Prior studies on radiation-induced tumors have shown a range of genomic effects and have suggested the involvement of various DNA DSB repair mechanisms^{30,32–35}. We identified a unique signature of RT-associated deletions carrying characteristics of DSB repair by c-NHEJ. This work extends our knowledge on the genomic response to RT and provides direction for the development of effective radiosensitizers.

The notable expansion of clones harboring RT-associated genomic events depends on clonal selection or drift³⁶. Therefore, the increased small-deletion burden in combination with poor outcomes may reflect the emergence of more competitive clones under RT-induced stress, innately active repair processes ensuring tumor

maintenance or a combination of these two. We found that a higher load of RT-associated deletions was linked to worse patient outcomes. Thus, additional rounds of RT in patients with recurrent or metastatic tumors containing a significant increase in small-deletion burden are unlikely to further extend progression-free survival. The ability to effectively repair RT-induced damage implies that sensitivity to RT is intrinsically diminished or has progressively been lost due to, for example, clonal selection. Inhibiting these repair processes could potentially sensitize tumors to the tumor-killing effect of ionizing radiation. *CDKN2A* homozygous deletions were acquired in RT⁺ *IDH*-mutant gliomas but not in RT⁻ recurrent *IDH*-mutant gliomas, suggesting that RT-induced DNA damage promotes the acquisition of this poor prognostic marker, and implicating a convergence between RT-induced DSB repair and cell cycle checkpoints. A biomarker able to readily detect an increased small-deletion burden may help reduce treatment costs and avoid RT-associated patient comorbidities and side effects.

We note several limitations to our study. The HMF metastatic dataset comprises samples from a single time point, preventing the attribution of alterations as post-treatment. Furthermore, the treatment annotation in HMF does not precisely describe whether only the initial tumor or additionally the metastatic site was also irradiated. Considering these caveats, the effects of RT described in this study might be more pronounced than what we have observed. Additionally, evolutionary pressures for local and distant metastases, which were analyzed homogeneously in this study, might be fundamentally different³⁷. RT may have no or a different impact on metastases that are not immediately within the field of the radiation, requiring further investigations in dedicated datasets.

Compounds that inhibit DNA repair may improve the response of cancer cells to RT. Numerous clinical and preclinical studies have shown efficacy in targeting DNA repair. Inhibitors directed at poly(ADP-ribose) polymerase (*PARP*) in HRD⁺ tumors (synthetic lethality) were shown to be effective in the treatment of various cancer types^{38–40}. Effective inhibitors of NHEJ have not yet been reported but may sensitize tumors to RT. Inhibitors of ATM serine/threonine kinase (*ATM*), a protein kinase that activates DSB repair; and DNA-dependent protein kinase catalytic subunit (*DNA-PKc*), a kinase that catalyzes repair at the DSB locus, were shown to be effective in preclinical studies and phase I trials of diffuse glioma^{41–44}. The identification of enrichment of APOBEC-associated mutational signatures may warrant further evaluation of targeting cytosine deaminases for cancer therapy⁴⁵. The present study highlights the importance of effective DNA repair in therapy resistance.

Online content

Any methods, additional references, Nature Research reporting summaries, source data, extended data, supplementary information, acknowledgements, peer review information; details of author contributions and competing interests; and statements of data and code availability are available at <https://doi.org/10.1038/s41588-021-00874-3>.

Received: 18 September 2020; Accepted: 21 April 2021;

Published online: 27 May 2021

References

- Barton, M. B. et al. Estimating the demand for radiotherapy from the evidence: a review of changes from 2003 to 2012. *Radiother. Oncol.* **112**, 140–144 (2014).
- Tyldesley, S. et al. Estimating the need for radiotherapy for patients with prostate, breast, and lung cancers: verification of model estimates of need with radiotherapy utilization data from British Columbia. *Int. J. Radiat. Oncol. Biol. Phys.* **79**, 1507–1515 (2011).
- Chang, H. H. Y., Pannunzio, N. R., Adachi, N. & Lieber, M. R. Non-homologous DNA end joining and alternative pathways to double-strand break repair. *Nat. Rev. Mol. Cell Biol.* **18**, 495–506 (2017).

4. Campbell, B. B. et al. Comprehensive analysis of hypermutation in human cancer. *Cell* **171**, 1042–1056 (2017).
5. Barthel, F. P. et al. Longitudinal molecular trajectories of diffuse glioma in adults. *Nature* **576**, 112–120 (2019).
6. Touat, M. et al. Mechanisms and therapeutic implications of hypermutation in gliomas. *Nature* **580**, 517–523 (2020).
7. Behjati, S. et al. Mutational signatures of ionizing radiation in second malignancies. *Nat. Commun.* **7**, 12605 (2016).
8. Priestley, P. et al. Pan-cancer whole-genome analyses of metastatic solid tumours. *Nature* **575**, 210–216 (2019).
9. Consortium, G. Glioma through the looking GLASS: molecular evolution of diffuse gliomas and the Glioma Longitudinal Analysis Consortium. *Neuro Oncol.* **20**, 873–884 (2018).
10. Stupp, R. et al. Radiotherapy plus concomitant and adjuvant temozolomide for glioblastoma. *N. Engl. J. Med.* **352**, 987–996 (2005).
11. Louis, D. N. et al. The 2016 World Health Organization Classification of Tumors of the Central Nervous System: a summary. *Acta Neuropathol.* **131**, 803–820 (2016).
12. Lutz, S. T., Jones, J. & Chow, E. Role of radiation therapy in palliative care of the patient with cancer. *J. Clin. Oncol.* **32**, 2913–2919 (2014).
13. Nguyen, L., Martens, J. W. M., Van Hoeck, A. & Cuppen, E. Pan-cancer landscape of homologous recombination deficiency. *Nat. Commun.* **11**, 5584 (2020).
14. Pich, O. et al. The mutational footprints of cancer therapies. *Nat. Genet.* **51**, 1732–1740 (2019).
15. Kucab, J. E. et al. A compendium of mutational signatures of environmental agents. *Cell* **177**, 821–836 (2019).
16. Georgakopoulos-Soares, I., Morganella, S., Jain, N., Hemberg, M. & Nik-Zainal, S. Noncanonical secondary structures arising from non-B DNA motifs are determinants of mutagenesis. *Genome Res.* **28**, 1264–1271 (2018).
17. Martincorena, I. et al. Universal patterns of selection in cancer and somatic tissues. *Cell* **171**, 1029–1041 (2017).
18. Alexandrov, L. B. et al. The repertoire of mutational signatures in human cancer. *Nature* **578**, 94–101 (2020).
19. Davies, H. et al. HRDetect is a predictor of *BRCA1* and *BRCA2* deficiency based on mutational signatures. *Nat. Med.* **23**, 517–525 (2017).
20. Touat, M. et al. Mechanisms and therapeutic implications of hypermutation in gliomas. *Nature* **580**, 517–523 (2020).
21. Nik-Zainal, S. et al. Landscape of somatic mutations in 560 breast cancer whole-genome sequences. *Nature* **534**, 47–54 (2016).
22. Roberts, S. A. et al. An APOBEC cytidine deaminase mutagenesis pattern is widespread in human cancers. *Nat. Genet.* **45**, 970–976 (2013).
23. Lei, L. et al. APOBEC3 induces mutations during repair of CRISPR–Cas9-generated DNA breaks. *Nat. Struct. Mol. Biol.* **25**, 45–52 (2018).
24. Nowarski, R. & Kotler, M. APOBEC3 cytidine deaminases in double-strand DNA break repair and cancer promotion. *Cancer Res.* **73**, 3494–3498 (2013).
25. Nowarski, R. et al. APOBEC3G enhances lymphoma cell radioresistance by promoting cytidine deaminase-dependent DNA repair. *Blood* **120**, 366–375 (2012).
26. Volkova, N. V. et al. Mutational signatures are jointly shaped by DNA damage and repair. *Nat. Commun.* **11**, 2169 (2020).
27. Ceccarelli, M. et al. Molecular profiling reveals biologically discrete subsets and pathways of progression in diffuse glioma. *Cell* **164**, 550–563 (2016).
28. Adewoye, A. B., Lindsay, S. J., Dubrova, Y. E. & Hurler, M. E. The genome-wide effects of ionizing radiation on mutation induction in the mammalian germline. *Nat. Commun.* **6**, 6684 (2015).
29. Bakhoun, S. F. et al. Numerical chromosomal instability mediates susceptibility to radiation treatment. *Nat. Commun.* **6**, 5990 (2015).
30. Rose, Li.Y. et al. Mutational signatures in tumours induced by high and low energy radiation in *Trp53* deficient mice. *Nat. Commun.* **11**, 394 (2020).
31. Touil, N., Elhajouji, A., Thierens, H. & Kirsch-Volders, M. Analysis of chromosome loss and chromosome segregation in cytokinesis-blocked human lymphocytes: non-disjunction is the prevalent mistake in chromosome segregation produced by low dose exposure to ionizing radiation. *Mutagenesis* **15**, 1–7 (2000).
32. Behjati, S. et al. Mutational signatures of ionizing radiation in second malignancies. *Nat. Commun.* **7**, 12605 (2016).
33. Davidson, P. R., Sherborne, A. L., Taylor, B., Nakamura, A. O. & Nakamura, J. L. A pooled mutational analysis identifies ionizing radiation-associated mutational signatures conserved between mouse and human malignancies. *Sci. Rep.* **7**, 7645 (2017).
34. Lopez, G. Y. et al. The genetic landscape of gliomas arising after therapeutic radiation. *Acta Neuropathol.* **137**, 139–150 (2019).
35. Phi, J. H. et al. Genomic analysis reveals secondary glioblastoma after radiotherapy in a subset of recurrent medulloblastomas. *Acta Neuropathol.* **135**, 939–953 (2018).
36. Hu, Z. et al. Quantitative evidence for early metastatic seeding in colorectal cancer. *Nat. Genet.* **51**, 1113–1122 (2019).
37. Reiter, J. G. et al. Lymph node metastases develop through a wider evolutionary bottleneck than distant metastases. *Nat. Genet.* **52**, 692–700 (2020).
38. Wiggans, A. J., Cass, G. K., Bryant, A., Lawrie, T. A., & Morrison, J. Poly(ADP-ribose) polymerase (PARP) inhibitors for the treatment of ovarian cancer. *Cochrane Database Syst. Rev.* **5**, CD007929 (2015).
39. Su, J. M. et al. A phase I trial of veliparib (ABT-888) and temozolomide in children with recurrent CNS tumors: a pediatric brain tumor consortium report. *Neuro Oncol.* **16**, 1661–1668 (2014).
40. O’Neil, N. J., Bailey, M. L. & Hieter, P. Synthetic lethality and cancer. *Nat. Rev. Genet.* **18**, 613–623 (2017).
41. Munster, P. et al. First-in-human phase I study of a dual mTOR kinase and DNA-PK inhibitor (CC-115) in advanced malignancy. *Cancer Manag. Res.* **11**, 10463–10476 (2019).
42. Goldberg, F. W. et al. The discovery of 7-methyl-2-[(7-methyl[1,2,4] triazolo[1,5-*a*]pyridin-6-yl)amino]-9-(tetrahydro-2*H*-pyran-4-yl)-7,9-dihydro-8*H*-purin-8-one (AZD7648), a potent and selective DNA-dependent protein kinase (DNA-PK) inhibitor. *J. Med. Chem.* **63**, 3461–3471 (2020).
43. Thijssen, R. et al. Dual TORC/DNA-PK inhibition blocks critical signaling pathways in chronic lymphocytic leukemia. *Blood* **128**, 574–583 (2016).
44. Timme, C. R., Rath, B. H., O’Neill, J. W., Camphausen, K. & Tofilon, P. J. The DNA-PK inhibitor VX-984 enhances the radiosensitivity of glioblastoma cells grown in vitro and as orthotopic xenografts. *Mol. Cancer Ther.* **17**, 1207–1216 (2018).
45. Li, M. et al. First-in-class small molecule inhibitors of the single-strand DNA cytosine deaminase APOBEC3G. *ACS Chem. Biol.* **7**, 506–517 (2012).

Publisher’s note Springer Nature remains neutral with regard to jurisdictional claims in published maps and institutional affiliations.

© The Author(s), under exclusive licence to Springer Nature America, Inc. 2021

Methods

Patient cohort. We curated a cohort of 190 patients with high-quality longitudinal DNA sequencing data, including treatment-naïve primary and matched post-treatment first-recurrence tumor samples from the GLASS dataset⁵. We classified paired samples according to the 2016 World Health Organization (WHO) classification into three subtypes: *IDH* mutant with 1p/19q co-deletion (*IDHmut-codel*), *IDH* mutant without 1p/19q co-deletion (*IDHmut-noncodel*) and *IDH* wild type (*IDHwt*)¹¹. The GLASS cohort used in this manuscript consists of $n = 106$ whole-genome sequencing samples ($n = 53$ primary samples, $n = 53$ matched first-recurrence samples) and $n = 274$ whole-exome sequencing samples ($n = 106$ primary samples, $n = 106$ matched first-recurrence samples). Detailed information on sequence platforms, capture kits and read length is outlined in the GLASS marker paper⁵.

For validation analyses, we curated a metastatic cohort from the HMF comprising a total of 4,549 samples⁸. The HMF cohort consists of metastatic tumor samples that were collected following local or systemic treatment as part of the CPCT-02 (NCT01855477) and DRUP (NCT02925234) clinical trials. Biopsy samples from a wide range of tumor types collected at various hospitals across the Netherlands were sequenced at the core facilities of the HMF. Whole-genome sequencing was performed for each sample according to standardized protocols¹⁶. Detailed information on sequence platforms, capture kits and read length is outlined in the HMF marker paper⁸. VCF files with mutations and associated metadata were downloaded from The Hartwig Medical Database (<https://database.hartwigmedicalfoundation.nl>). After application of filtering criteria using BCFTools 1.9 (as described in detail in Extended Data Fig. 1e), a set of $n = 3,693$ were defined and used for the majority of analyses throughout the manuscript. For survival analyses, we selected RT⁺ samples with sufficient survival information ($n = 958$). All prior RT data were extracted using clinical data as present in the CPCT-02 eCRF on 8 December 2020. These data were not cleaned and represent the data entered by the clinical sites. The prior RT was categorized as curative intent, palliative intent or other. All other instances were manually curated by the principal investigator. All adjuvant/neo-adjuvant or post-operative RT was considered curative intent RT. All local RT for pain relief or other symptom-directed goals was considered as palliative. Some items were not specified, and those events were not included in our analysis. We also excluded all RT for non-malignant disease states, specifically for gynecostasia treatment after castration. We cannot exclude overrepresentation or underrepresentation of the radiation signatures as we are unaware whether the metastases that were biopsied were not already present at the time of RT.

Variant calling. Variant calling in the GLASS dataset was performed according to the GATK best practices using GATK 4.1.0.0 and publicly released as part of a previous publication⁵. Briefly, GATK 4.1. was used for variant calling in tumor samples against a matched normal control. Additionally, panels of normals were constructed across multiple control samples from the same tissue source and sequencing center. Variants were broadly filtered for germline variants, cross-sample contamination, read orientation and sequence context. Variants were called across all samples for a given patient. Variants with a minimum coverage of 10 reads in both primary and recurrence and a minimum variant allele frequency of 10% for either the primary or the recurrence were included for further analysis. Variants were considered to be present if at least one mutant read was detected in a sample. Mutations directly overlapping with known repeat regions according to the repeatmasker database were removed. Specifically, we filtered out all variants in known repeat regions, including DNA satellites, microsatellites, long terminal repeats, transposable elements (LINE/SINE elements) and low-complexity regions. Variant clonality was inferred for each patient individually using PyClone (v.0.13.1) and as described in more detail in the GLASS marker paper.

Mutation burden comparison. The mutation burden was calculated as the number of mutations per megabase with at least 10× coverage and stratified by variant type. The overall tumor mutation burden was calculated as the sum of the burden of small deletions, small insertions and SNVs. Recurrent tumors with greater than 10 mutations per megabase were considered hypermutated as previously described⁵. For the comparison of mutation burden between RT treatment groups in the GLASS dataset, we calculated the burden of mutations unique to the recurrent tumors and therefore acquired after treatment. To adjust for confounding covariables, we fitted a multivariable log-linear regression model using the *glm* function in R. In addition to RT treatment, we included TMZ treatment, hypermutation, surgical interval in months and molecular subtype as variables. The small-deletion burden in the GLASS dataset was not confounded by batch effects. Accordingly, we included the full therapy and tumor type information for mutation burden analyses in the Hartwig metastatic cohort. To adjust for negative infinite values resulting from the log transformation in the GLASS cohort, we added a constant value of 1 to the log function. For the metastatic cohort, the log transformation did not result in (negative) infinite values and therefore did not necessitate the addition of a constant value.

Association of deletions with non-B-DNA structures. The genomic locations of non-canonical DNA structures were derived from the Non-B DNA database⁴⁷. We calculated for every variant position and, for comparison, for 250,000 randomly

sampled positions from the reference genome, the distance to non-B features as a continuous (absolute distance to genomic feature in base pairs) or categorical (position in or up to 100 bp to genomic feature—yes/no) value. We used a two-sided Mann–Whitney *U* test for differences in the genomic properties of variants in radiation-induced and non-radiation-induced tumors after adjusting for random background distribution.

dNdScv. For quantification of selection processes at the level of individual genes dependent on RT, we calculated dN/dS ratios as previously described⁴. Briefly, the R package dNdScv¹⁷ was run using the default and recommended parameters for each mutational fraction (private to primary, shared between primary and recurrence and private to recurrence). All analyses were conducted separately within RT-naïve and RT-treated groups.

Sequence microhomology. Sequence microhomology was determined by iteratively comparing the 3' end of the deleted sequence to the 5' flanking sequence. Any deletion demonstrating at least 2 nucleotides of homology was considered microhomology mediated. The homologous sequence was characterized and further analyzed for the presence of 1-, 2- and 3-nucleotide repeats. The repeat unit and number of repeats were quantified.

Mutational signatures. SigProfiler was used to extract and plot mutational signatures of SBSs, double-base substitutions and indels¹⁸. Absolute and relative contributions of signatures were determined using modified functions from the MutationalPatterns R package⁴⁸. Briefly, we fitted the mutational profile matrix generated with SigProfiler to the catalog of previously identified COSMIC mutational signatures (v3, May 2019) by solving the non-negative least-squares problem. The SBS signatures SBS31 and SBS35 have previously been linked to platinum therapy^{14,18}. Analysis of the HMF cohort using the signatures we extracted confirmed these previously established associations, providing further credence to the identified signatures. SigProfilerPlotting⁴⁹ was used to visualize the distribution of indel characteristics (Extended Data Fig. 3a–d).

Structural variants. For the GLASS dataset, split reads and discordant read pairs were extracted from all tumor and normal BAM files using samtools 1.7⁵⁰. We used the lumpyexpress tool (from LUMPY 0.2.13) to call structural variants providing the data associated with the set of normal and tumor samples belonging to one patient⁵¹. Copy number variation predictions inferred from read depth using CNVator 0.3.3 were additionally provided to garner further support for identified variants⁵². The resulting call set was post-processed using SVtyper 0.6.0 to genotype structural variants for each individual sample belonging to a patient⁵³. Finally, we used GATK VariantFiltration to filter all variants with fewer than four reads of support and those with quality scores less than ten⁵⁴. Variants that showed any support in non-tumor samples were additionally removed. Variants were quantified per sample and further stratified according to type (translocation, duplication, deletion and inversion). We computed the change in frequencies for each patient by dividing the rate at recurrence by the rate at primary. Only variants spanning at least 20 bp were considered.

MSI and HRD. MSI and HRD status were assigned according to previously defined criteria¹³. In short, MSI was determined in samples with >14,000 indel repeats; HRD was classified on the basis of a probability score of ≥ 0.5 according to the CHORD algorithm.

Aneuploidy calculation. Arm-level aneuploidy data from the GLASS dataset were obtained from a previous publication and copy number segmentation files from HMF were processed into arm-level copy number calls using the same methods⁵. Chromosomes demonstrating euploidy in both arms were considered euploid. Chromosomes with equidirectional aneuploidy in both arms or aneuploidy in a single arm and indeterminate ploidy in the other arm were considered simple aneuploid. Chromosomes with aneuploidy in one arm and incongruent ploidy in the other arm were considered complex aneuploid. Aneuploidy events were quantified for each tumor sample.

Statistical methods. All data analyses were conducted in R 3.6.1 (broadly using tidyverse 1.3.0), Python 3.7.3 and PostgreSQL 10.5. R was interfaced with the PostgreSQL database used for data storage using the unixODBC 2.3.6 driver plus the DBI 1.0.0 and odbc 1.1.6 R packages. All survival analyses including Kaplan–Meier plots and Cox proportional hazards models were conducted using the R packages survival and survminer. For unpaired group comparisons, the two-sided Mann–Whitney *U* test and two-sided Kruskal–Wallis test were used and for paired longitudinal comparisons the two-sided Wilcoxon signed-rank test was applied. Forest plots were generated using the R package forestmodel. Survival times for the GLASS dataset were calculated as described previously⁵. In the HMF metastatic cohort, we calculated survival starting from the date of biopsy to date of death. For patients that were alive, we used the last date of follow-up (date of treatment end) as censoring.

Reporting Summary. Further information on research design is available in the Nature Research Reporting Summary linked to this article.

Data availability

Processed sequencing data from the GLASS project used in this study are available on Synapse, at <https://www.synapse.org/glass>. The whole-genome sequencing, RNA sequencing and corresponding clinical data used in this study were made available by the HMF and were accessed under a license agreement (HMF DR-057 version 3.0). Data access can be obtained by filling out a data request form. The form and detailed application procedures can be found at <https://www.hartwigmedicalfoundation.nl/applying-for-data/>. The repeatmasker database used in this manuscript is available at <https://www.repeatmasker.org/>.

Code availability

Pipeline scripts can be found at <https://github.com/fparthel/GLASS>. Custom scripts for analyses performed in this manuscript can be found at <https://github.com/EmreKocakavuk/RTscars>.

References

46. Bins, S. et al. Implementation of a multicenter biobanking collaboration for next-generation sequencing-based biomarker discovery based on fresh frozen pretreatment tumor tissue biopsies. *Oncologist* **22**, 33–40 (2017).
47. Cer, R. Z. et al. Non-B DB v2.0: a database of predicted non-B DNA-forming motifs and its associated tools. *Nucleic Acids Res.* **41**, D94–D100 (2013).
48. Blokzijl, F., Janssen, R., van Boxtel, R. & Cuppen, E. MutationalPatterns: comprehensive genome-wide analysis of mutational processes. *Genome Med.* **10**, 33 (2018).
49. Bergstrom, E. N. et al. SigProfilerMatrixGenerator: a tool for visualizing and exploring patterns of small mutational events. *BMC Genomics* **20**, 685 (2019).
50. Li, H. et al. The Sequence Alignment/Map format and SAMtools. *Bioinformatics* **25**, 2078–2079 (2009).
51. Layer, R. M., Chiang, C., Quinlan, A. R. & Hall, I. M. LUMPY: a probabilistic framework for structural variant discovery. *Genome Biol.* **15**, R84 (2014).
52. Abyzov, A., Urban, A. E., Snyder, M. & Gerstein, M. CNVnator: an approach to discover, genotype, and characterize typical and atypical CNVs from family and population genome sequencing. *Genome Res.* **21**, 974–984 (2011).
53. Chiang, C. et al. SpeedSeq: ultra-fast personal genome analysis and interpretation. *Nat. Methods* **12**, 966–968 (2015).
54. Van der Auwera, G. A. et al. From FastQ data to high confidence variant calls: the Genome Analysis Toolkit best practices pipeline. *Curr. Protoc. Bioinformatics* **43**, 11.10.1–11.10.33 (2013).

Acknowledgements

This publication and the underlying study have been made possible partly on the basis of the data that HMF and the Center of Personalised Cancer Treatment (CPCT) have made available to the study. This work was supported by the NIH grants R01 CA190121, R01 CA237208, R21 NS114873 and Cancer Center Support Grant P30 CA034196, grants from the Musella Foundation, the B*CURVED Foundation and the Brain Tumour Charity, and the Department of Defense W81XWH1910246 (R.G.W.V.). F.P.B. is supported by the JAX Scholar program and the National Cancer Institute (K99 CA226387). F.S.V. is supported by a postdoctoral fellowship from The Jane Coffin Childs Memorial Fund for Medical Research. K.C.J. is the recipient of an American Cancer Society Fellowship (130984-PF-17-141-01-DMC). E.K. is the recipient of an MD fellowship by the Boehringer Ingelheim Fonds and is supported by the German National Academic Foundation.

Author contributions

E.K., F.P.B. and R.G.W.V. designed the project. Data processing and analysis was performed by E.K. and F.P.B.; data visualization was performed by E.K., E.K., K.J.A., F.S.V., K.C.J., S.B.A., F.P.B. and R.G.W.V. participated in the design of analyses and interpretation of results. M.P.L. provided clinical data. E.K., F.P.B. and R.G.W.V. wrote the manuscript. All coauthors including M.P.L. and E.P.S. discussed the results and commented on the manuscript.

Competing interests

R.G.W.V. is a co-founder of Boundless Bio, Inc., which was not involved in the research presented here. R.G.W.V. is a member of the Scientific Advisory Board of the HMF. F.P.B. has performed consulting for Bristol Myers Squibb. R.G.W.V., E.K., K.J.A. and F.P.B. are listed as inventors on a patent application filed by The Jackson Laboratory, related to the findings described here. The remaining authors declare no competing interests.

Additional information

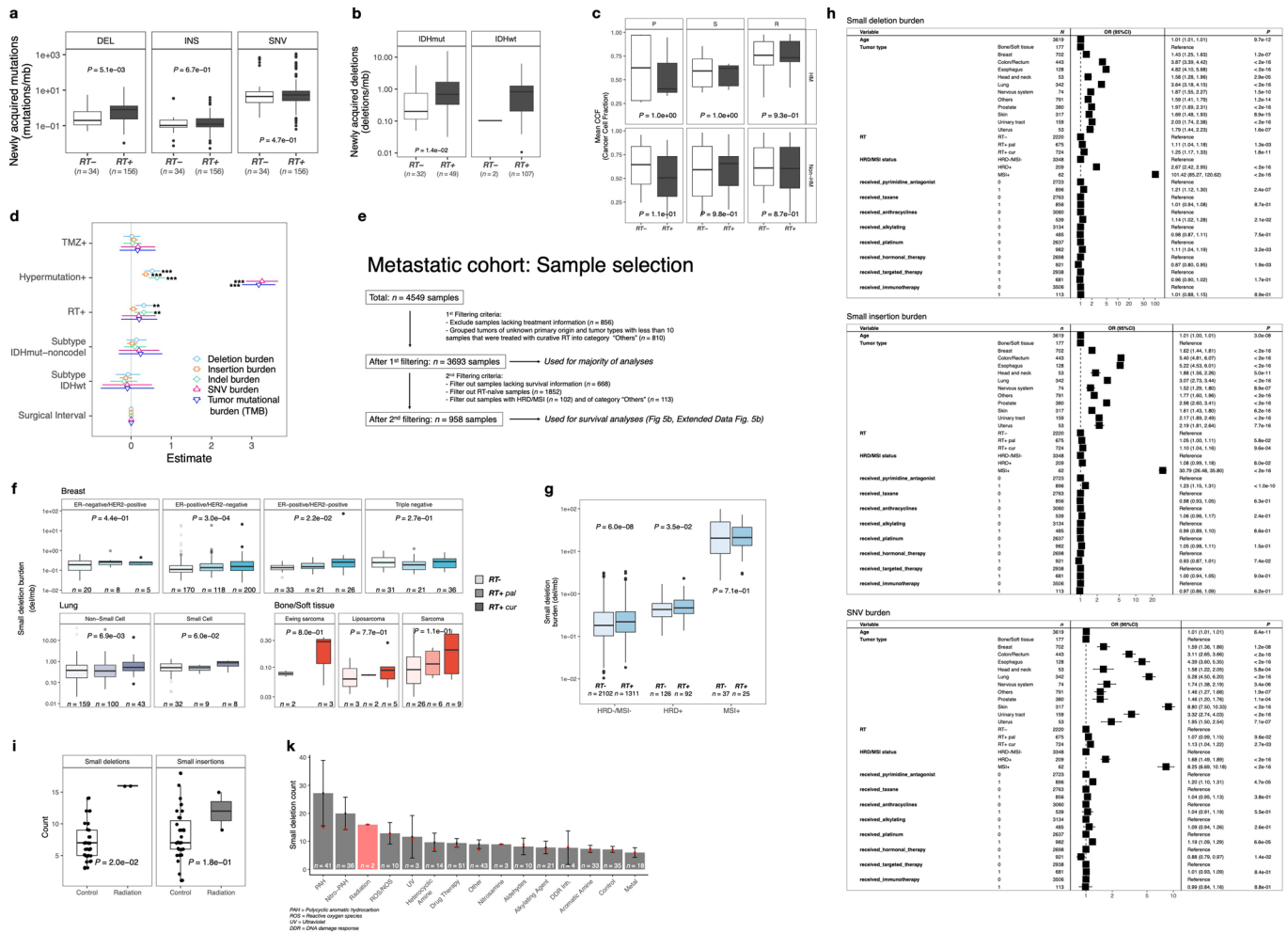
Extended data is available for this paper at <https://doi.org/10.1038/s41588-021-00874-3>.

Supplementary information The online version contains supplementary material available at <https://doi.org/10.1038/s41588-021-00874-3>.

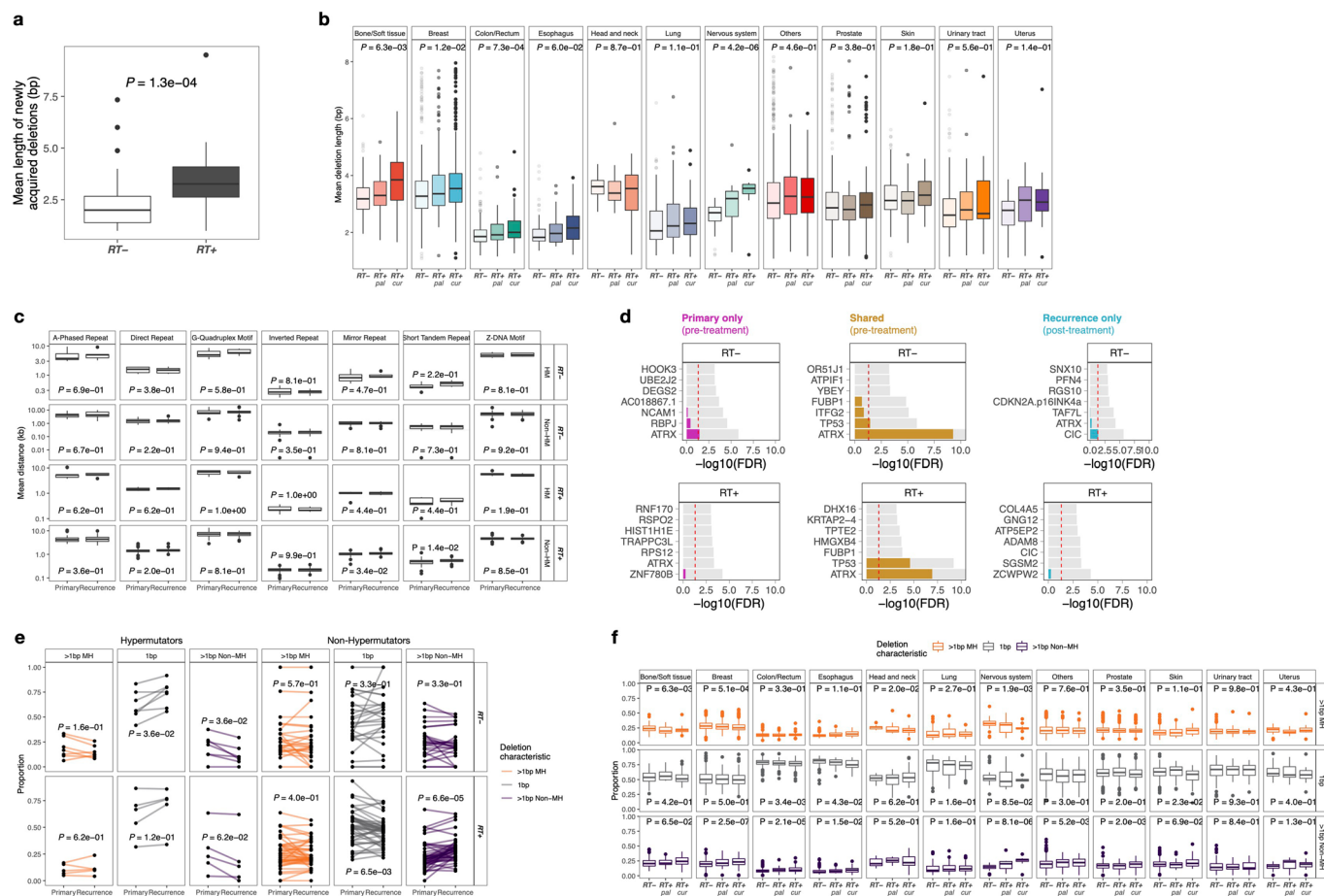
Correspondence and requests for materials should be addressed to F.P.B. or R.G.W.V.

Peer review information *Nature Genetics* thanks Moritz Gerstung, Simon Powell and the other, anonymous, reviewer(s) for their contribution to the peer review of this work. Peer reviewer reports are available.

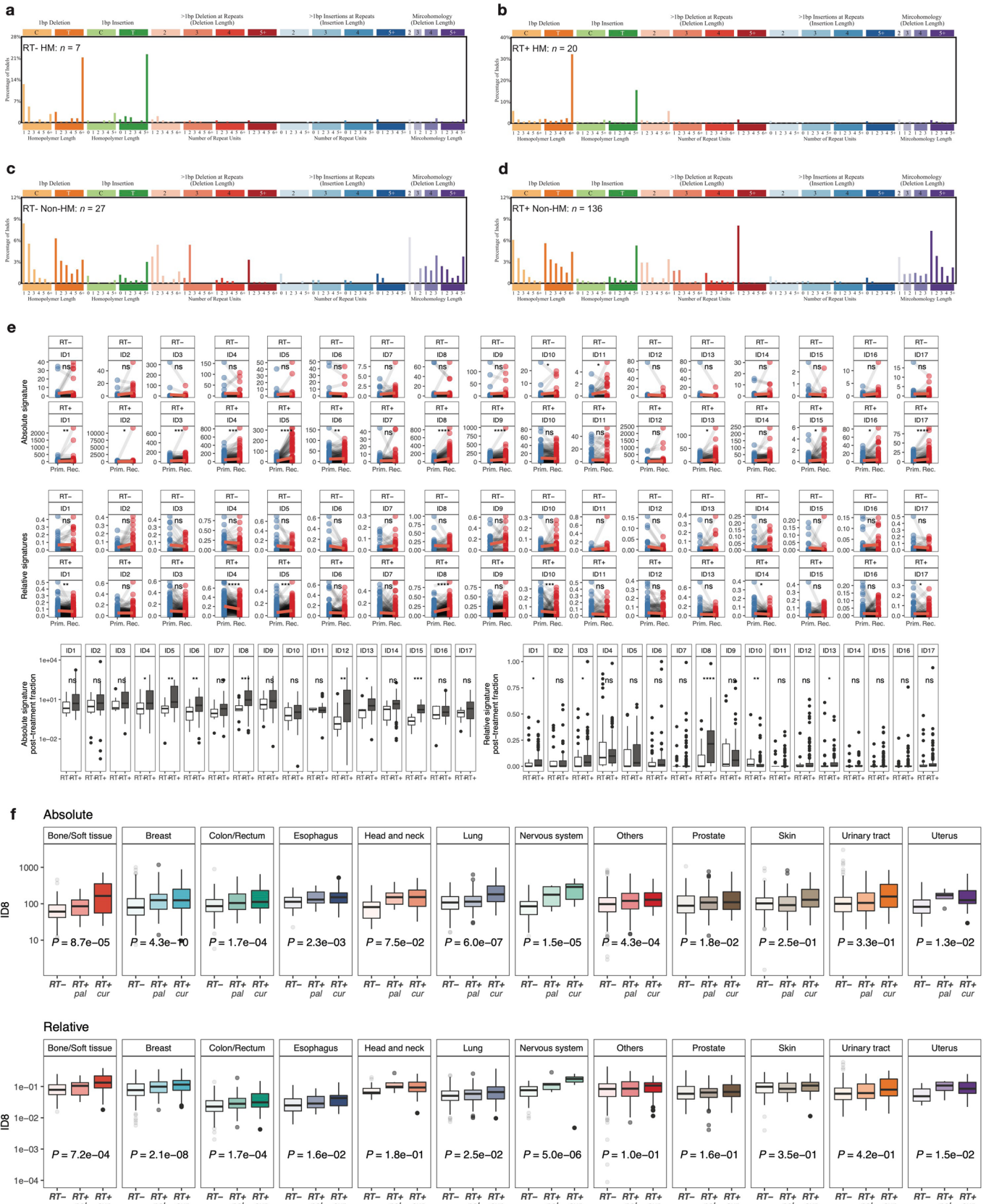
Reprints and permissions information is available at www.nature.com/reprints.



Extended Data Fig. 1 | Radiotherapy specifically drives small deletion burden independent of multiple variables. **a**, Boxplot (in this and all following figures: boxes span quartiles, center lines as medians, whiskers represent absolute range, excluding outliers): burden of post-treatment mutations (mutations/mb) in RT-naïve (n = 34) and RT-received (n = 156) patients from GLASS cohort. Mutations separated by DEL (deletions), INS (insertions) and SNV (single nucleotide variants). Two-sided Mann-Whitney U test. **b**, Acquired small deletion burden comparison between RT-naïve and RT-received cases separated by molecular subtype. Two-sided Mann-Whitney U test. **c**, Comparison of mean cancer cell fraction of small deletions per patient in GLASS separated by P, primary-only fraction, S, shared fraction and R, recurrence-only fraction and by HM, hypermutation. Two-sided Mann-Whitney U test. **d**, Forest plots: multivariable log-linear regression model of acquired mutation burden (mutations/mb) in GLASS. Point, mean estimate; lines, 95%-confidence-interval. Two-sided t-test (**=p < 0.01, ***=p < 0.001). **e**, Sample selection and filtering criteria for HMF including a detailed description of the usage for specific figures. **f**, Separation of lung, breast and bone/soft tissue cancers into respective subtypes. Comparison of small deletion burden between RT-, RT + pal and RT + cur samples. Two-sided Kruskal-Wallis test. **g**, Boxplots depicting burden of small deletions in HRD-/MSI- (n = 3,413), HRD+ (n = 218) and MSI+ (n = 62) samples from the HMF cohort separated by RT-status. Two-sided Mann-Whitney U test. **h**, Forest plots depicting multivariable log-linear regression model for mutation burdens in HMF. Two-sided t-test. Mutations separated into small deletions/insertions and SNVs. Independent variables: age, primary tumor location, DNA repair deficiency background and treatment including radiotherapy, taxane, alkylating agents, platin and others. **i**, Comparison of small deletion counts between control vs ionizing radiation groups (PMID:30982602). Two-sided Mann-Whitney U test. **j**, Distribution of small deletion counts per treatment group (PMID:30982602). Data presented as mean values +/- standard error of the mean, and red dots indicate median count of small deletions.

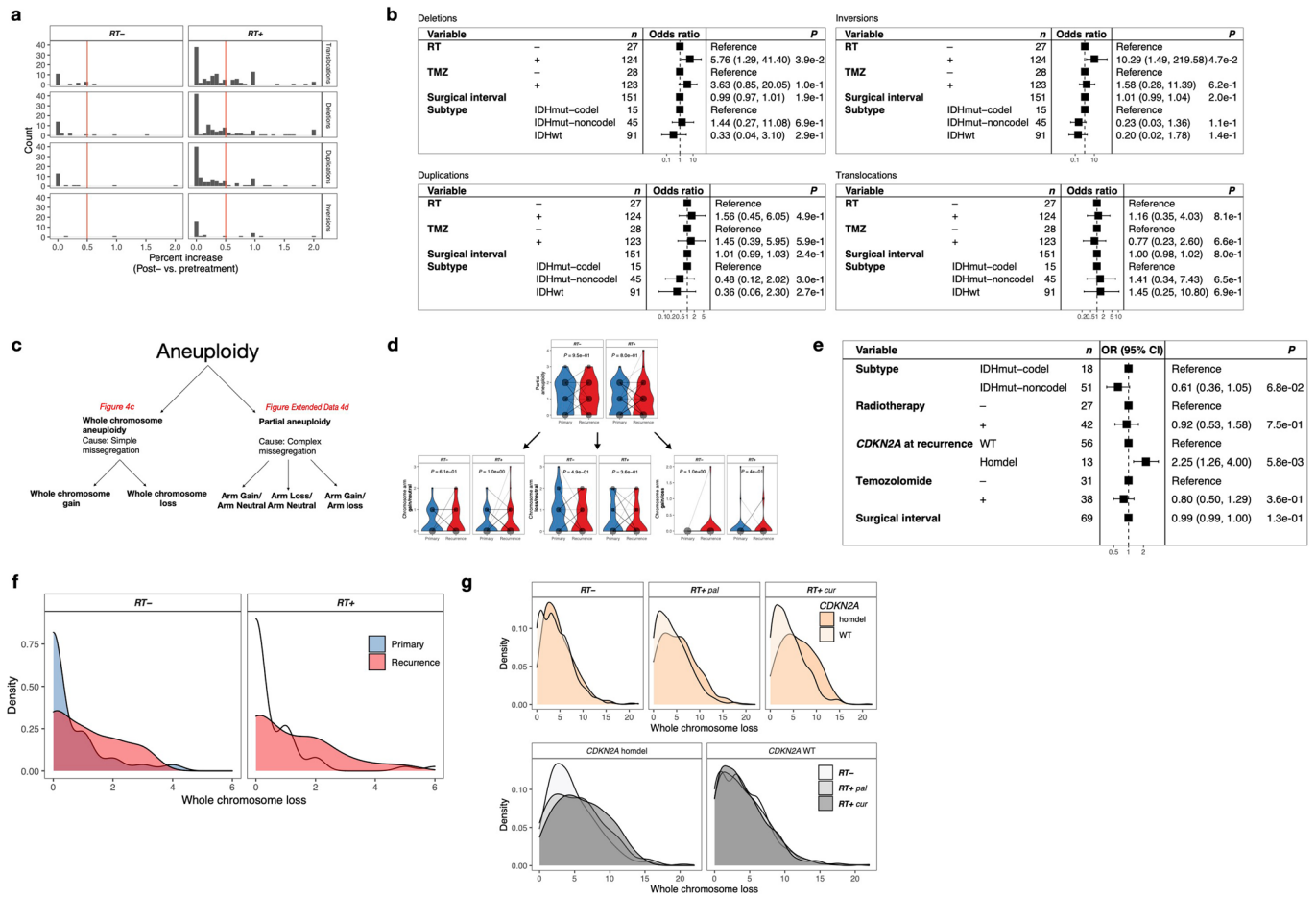


Extended Data Fig. 2 | Genomic characteristics of RT-associated small deletions. **a**, Comparison of mean deletion lengths of acquired deletions in RT- vs RT+ *IDHmut* gliomas. Two-sided Mann-Whitney *U* test. **b**, Metastatic cohort: Boxplots depicting mean deletion lengths in RT-naïve (left) and palliative RT-treated (middle) and curative RT-treated (right) tumor samples separated by primary tumor location. Two-sided Kruskal-Wallis test. **c**, Longitudinal comparison (X-Axis) of mean distances of deletions to non-B DNA features in kb (Y-Axis) in *IDHmut* glioma cases. Cases separated by radiation treatment and hypermutation. Note that neither in hypermutated, nor in RT-naïve non-hypermutated glioma samples significant longitudinal differences were observed. Two-sided paired Wilcoxon signed-rank test. **d**, Gene-wise dN/dS estimates by RT (rows) and fraction (columns) in GLASS. Two-sided likelihood ratio tests. Genes sorted by Q-value (Bonferroni-adjusted P-value) and P-value. Q-values indicated in color, whereas P-values shown in light grey. Q-value threshold of 0.05 indicated by a horizontal red line. **e**, Comparison of proportion of deletions for *IDHmut* glioma samples separated by RT and hypermutation. Two-sided paired Wilcoxon signed-rank test. For each sample, the proportion of deletions with 1 bp length, > 1 bp length with microhomology and > 1 bp length without microhomology add up to 1. Bottom right panels (RT-received non-hypermutators) presented in Fig. 2d and shown here for comparison with other groups. **f**, Comparison of proportion of deletions in metastatic cohort between RT-treated and RT-naïve cases using two-sided Kruskal-Wallis test. In bone/soft tissue, breast and head & neck and nervous system cancers, significantly lower proportions of deletions > 1 bp with microhomology were observed in RT-treated samples compared to RT-naïve samples. In contrast, RT-received breast, colon/rectum, esophagus, nervous system and prostate tumor samples showed significantly higher proportions in deletions > 1 bp without microhomology. Boxes span quartiles, center lines as medians, whiskers represent absolute range, excluding outliers.

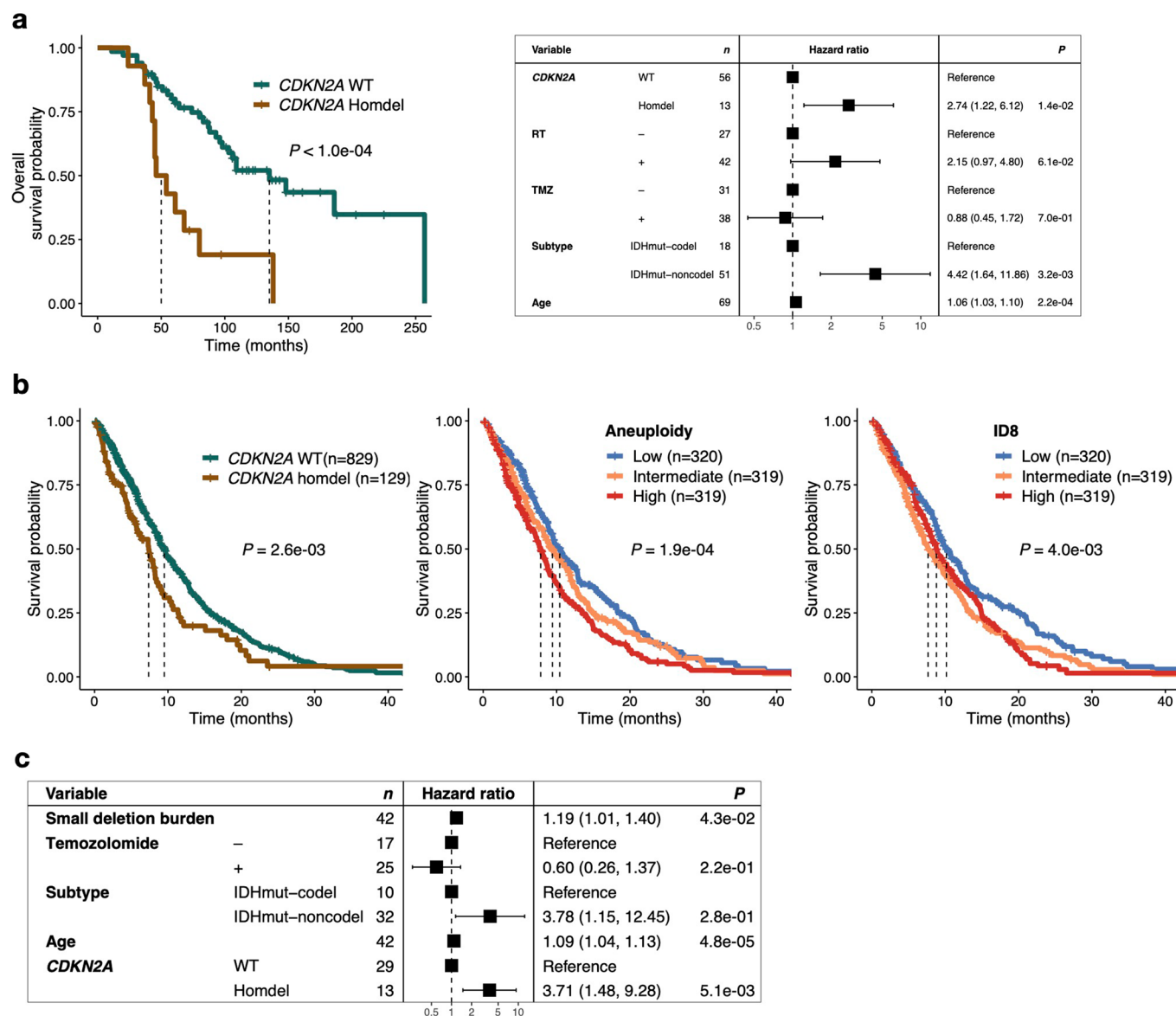


Extended Data Fig. 3 | See next page for caption.

Extended Data Fig. 3 | Mutational signatures associated with RT. **a-d**, Distribution of indel types for post-treatment mutations in the GLASS cohort, separated by RT (**a, c**, RT- negative; **b, d**, RT-treated) and HM (**a-b**, Hypermutator; **c-d**, Non-Hypermutator). Note that patterns of indels in hypermutated samples resemble the previously identified MSI signature ID2, whereas RT-treated Non-Hypermutant gliomas harbor large similarities with ID8. Sample sizes for each subgroup are annotated. **e**, Comprehensive comparison of all 17 COSMIC indel (ID) signatures in *IDH*mut glioma. Top 2 panels display longitudinal comparison of absolute signature contributions separated by radiation treatment (RT+ and RT-). Middle 2 panels display longitudinal comparison of relative signature contributions separated by radiation treatment. For these panels two-sided paired Wilcoxon signed-rank test was applied for statistical testing. Bottom panels display comparison of absolute (left) and relative (right) signatures of post-treatment indels between RT-treated and RT-naïve samples. For these panels two-sided Mann-Whitney U test was applied for statistical testing. (ns = not significant, * = $p < 0.05$, ** = $p < 0.01$, *** = $p < 0.001$, **** = $p < 0.0001$). Note that ID8 is the only signature consistently associated with radiation therapy across different comparisons, nominating it as a robust signature of radiotherapy. Boxes span quartiles, center lines as medians, whiskers represent absolute range, excluding outliers. **f**, Absolute (top) and relative (bottom) contribution of ID8 signature in metastatic cohort compared between cases with prior radiation treatment and cases without prior radiation treatment separated by tumor types. Note that most tumor types show significantly higher values of the signature in curative RT+ cases. Two-sided Kruskal-Wallis test was applied for statistical testing. Boxes span quartiles, center lines as medians, whiskers represent absolute range, excluding outliers.



Extended Data Fig. 4 | Effects of radiotherapy on structural variants. **a**, Analysis of structural variants (SVs) in glioma samples (Translocations, Duplications, Deletions, Inversions). For each patient, number of SVs were calculated pre-and post-treatment and the proportional increase after therapy for each SV-type was plotted separately for RT-naïve and RT-treated samples. Based on the distribution of proportional increase from primary to recurrence, a cutoff was defined for >50% increase that was further used for analyses in Fig. 4a. **b**, To support analyses presented in Fig. 4a, a multivariable logistic regression model was fitted for the >50% increase values of the structural variant types. Two-sided Wald test. This model includes radiation therapy, temozolomide therapy, molecular subtype and surgical interval as variables. **c**, Schematic overview of separation of aneuploidy events into whole chromosome aneuploidy as a result of simple segregation errors and partial aneuploidy as a result of complex segregation errors. **d**, Longitudinal analysis of partial aneuploidy in *IDHmut* glioma samples. Dots are proportional to the frequency of whole chromosome loss integer for each subgroup. Two-sided paired Wilcoxon rank-signed test. **e**, Multivariable Poisson regression model for whole chromosome losses in *IDHmut* glioma including molecular subtype, RT, TMZ, surgical interval and *CDKN2A* status at recurrence as variables. Two-sided Wald test. Note that *CDKN2A* homdel, but not RT is independently associated with higher whole chromosome losses. **f**, Density plots over integers of whole chromosome deletion scores for comparison between primary vs recurrent glioma samples, separated by radiotherapy. **g**, Density plots over integers of whole chromosome deletion scores for comparison between RT-naïve vs RT + pal vs RT + cur and/or *CDKN2A* homdel vs. wild-type (WT) samples from the HMF dataset. Note that *CDKN2A* homdel is associated with higher whole chromosome deletion scores, independent of RT. Within samples with *CDKN2A* homdel, samples that were RT-treated with curative intent show the highest deletion scores.



Extended Data Fig. 5 | Radiotherapy-associated genomic scars linked to poor survival. **a**, Left: Kaplan-Meier survival plot comparing overall survival time dependent on *CDKN2A* status at recurrence using two-sided log-rank test in *IDH* mutant glioma samples. Right: Multivariable cox regression model including *CDKN2A* status at recurrence, TMZ-treatment, molecular subtype and Age as variables. Two-sided Wald test was applied. **b**, Left: Kaplan Meier survival plot comparing survival time dependent on *CDKN2A* status at metastasis using two-sided log-rank test in RT-treated metastases (n=958 with available survival information). Middle: Kaplan Meier survival plot comparing survival time dependent on aneuploidy burden at metastasis using two-sided log-rank test in RT-treated metastases (n=958 with available survival information). Samples were separated into 3 tertiles based on whole chromosome loss aneuploidy scores: high (top tertile), intermediate (middle tertile) and low (bottom tertile). Right: Kaplan Meier survival plot comparing survival time dependent RT signature ID8 burden at metastasis using two-sided log-rank test in RT-treated metastases (n=958 with available survival information). Samples were separated into 3 tertiles based on ID8 burden: high (top tertile), intermediate (middle tertile) and low (bottom tertile). Note that a low ID8 burden is associated with better survival, indicating a better response to RT. **c**, Multivariable cox regression model including deletion burden at recurrence as continuous variable, *CDKN2A* homozygous deletion, Temozolomide-treatment, molecular subtype and age as variables in RT-treated *IDH* mutant samples.

Reporting Summary

Nature Research wishes to improve the reproducibility of the work that we publish. This form provides structure for consistency and transparency in reporting. For further information on Nature Research policies, see our [Editorial Policies](#) and the [Editorial Policy Checklist](#).

Statistics

For all statistical analyses, confirm that the following items are present in the figure legend, table legend, main text, or Methods section.

n/a Confirmed

- The exact sample size (n) for each experimental group/condition, given as a discrete number and unit of measurement
- A statement on whether measurements were taken from distinct samples or whether the same sample was measured repeatedly
- The statistical test(s) used AND whether they are one- or two-sided
Only common tests should be described solely by name; describe more complex techniques in the Methods section.
- A description of all covariates tested
- A description of any assumptions or corrections, such as tests of normality and adjustment for multiple comparisons
- A full description of the statistical parameters including central tendency (e.g. means) or other basic estimates (e.g. regression coefficient) AND variation (e.g. standard deviation) or associated estimates of uncertainty (e.g. confidence intervals)
- For null hypothesis testing, the test statistic (e.g. F , t , r) with confidence intervals, effect sizes, degrees of freedom and P value noted
Give P values as exact values whenever suitable.
- For Bayesian analysis, information on the choice of priors and Markov chain Monte Carlo settings
- For hierarchical and complex designs, identification of the appropriate level for tests and full reporting of outcomes
- Estimates of effect sizes (e.g. Cohen's d , Pearson's r), indicating how they were calculated

Our web collection on [statistics for biologists](#) contains articles on many of the points above.

Software and code

Policy information about [availability of computer code](#)

Data collection

PostgreSQL 10.5 (data collection and storage, data analysis)
DBI (R package) version: 1.0.0 (database management)
odbc (R package) version 1.1.6 (database connectivity)
unixODBC 2.3.6 (database connectivity)

Data analysis

BCFTools 1.9 (normalize, sort and index variants)
 snakemake 5.2.2 (pipeline development)
 GATK (including Mutect2) version: 4.1.0.0 (SNV/CNV detection)
 samtools 1.7 (sam/bam processing)
 SigProfilerMatrixGenerator version: 1.1 (mutational signatures)
 SigProfilerPlotting version: 1.1 (mutational signatures)
 MutationalPatterns version: 1.6.1 (mutational signatures)
 lumpy version: 0.2.13 (calling structural variants)
 CNVnator version: 0.3.3 (copy number variations)
 SVtyper version: 0.6.0 (post-processing structural variant calls)
 PyClone version: 0.13.1 (cancer cell fraction)
 dndscv (R package) version: 0.0.1.0 (selection strength, nominate driver genes)
 tidyverse (R package) version: 1.3.0 (data analysis and visualization)
 survival (R package) version: 3.1-12 (survival analyses)
 survminer (R package) version 0.4.6 (survival analysis)
 forestmodel (R package) version: 0.5.0 (visualization forest plots)
 All custom scripts relevant to this paper can be found on our github page at <https://github.com/EmreKocakavuk/RTscars>. Data pre-processing pipelines can be found at <https://github.com/fpbarthel/GLASS>.

For manuscripts utilizing custom algorithms or software that are central to the research but not yet described in published literature, software must be made available to editors and reviewers. We strongly encourage code deposition in a community repository (e.g. GitHub). See the Nature Research [guidelines for submitting code & software](#) for further information.

Data

Policy information about [availability of data](#)

All manuscripts must include a [data availability statement](#). This statement should provide the following information, where applicable:

- Accession codes, unique identifiers, or web links for publicly available datasets
- A list of figures that have associated raw data
- A description of any restrictions on data availability

Processed sequencing data from the GLASS project used in this study are available on Synapse, at <https://www.synapse.org/glass>. The WGS, RNA-seq, and corresponding clinical data used in this study were made available by the Hartwig Medical Foundation and were accessed under a license agreement (HMF DR-057 version 3.0). Data access can be obtained by filling out a data request forms. The form and detailed application procedures can be found online at <https://www.hartwigmedicalfoundation.nl/applying-for-data/>. The repeatmasker database used in this manuscript is available online at <https://www.repeatmasker.org/>.

Field-specific reporting

Please select the one below that is the best fit for your research. If you are not sure, read the appropriate sections before making your selection.

Life sciences Behavioural & social sciences Ecological, evolutionary & environmental sciences

For a reference copy of the document with all sections, see [nature.com/documents/nr-reporting-summary-flat.pdf](https://www.nature.com/documents/nr-reporting-summary-flat.pdf)

Life sciences study design

All studies must disclose on these points even when the disclosure is negative.

Sample size	No statistical methods were used to predetermine sample size. This is a retrospective analysis and all available data was initially included to maximize sample size and power. A detailed sample selection is described in the "Data exclusions" section below.
Data exclusions	GLASS: From the high-quality longitudinal DNA sequencing data of n=222, we selected matched samples from primary and matched first recurrence glioma samples from n=190 patients (n=380 samples) with fully annotated clinical information on radiotherapy treatment and survival data. HMF: We downloaded WGS data from 4549 metastatic samples from the Hartwig Medical Foundation. We applied 2 major filtering steps. First, we excluded samples lacking treatment information (n=856), and grouped tumors of unknown origin of primary tumor and tumor types with less than n=10 samples that were treated with curative RT into the category "Others" (n=810). After application of filtering criteria (as described in detail in Supplementary Fig. 1e) a set of 3693 samples were defined and used for the majority of analyses throughout the manuscript. In a second filtering step, we excluded samples lacking treatment information (n=668) and filtered out samples that were radiotherapy-naïve (n=1852), harbored homologous recombination deficiency (HRD) or microsatellite instability (MSI) backgrounds (n=102) or were categorized as "Others" as described above (n=113). We used the curated n=958 samples with radiotherapy treatment and sufficient survival information for survival analyses.
Replication	Findings were found to be consistent in two independent datasets. Furthermore, data and code are available as outlined above and execution of this code on the matching dataset will accurately reproduce the noted findings.
Randomization	There was no randomization in this work. This work is a retrospective analysis and does not concern a controlled trial where patients or samples are assigned to an intervention group.
Blinding	All patient samples were deidentified and were assigned a study-specific barcode. This concerns a retrospective study and blinding was not relevant to our work as patients were not randomly assigned to an intervention group.

Reporting for specific materials, systems and methods

We require information from authors about some types of materials, experimental systems and methods used in many studies. Here, indicate whether each material, system or method listed is relevant to your study. If you are not sure if a list item applies to your research, read the appropriate section before selecting a response.

Materials & experimental systems

Methods

- | n/a | Involvement in the study |
|-------------------------------------|--|
| <input checked="" type="checkbox"/> | <input type="checkbox"/> Antibodies |
| <input checked="" type="checkbox"/> | <input type="checkbox"/> Eukaryotic cell lines |
| <input checked="" type="checkbox"/> | <input type="checkbox"/> Palaeontology and archaeology |
| <input checked="" type="checkbox"/> | <input type="checkbox"/> Animals and other organisms |
| <input checked="" type="checkbox"/> | <input type="checkbox"/> Human research participants |
| <input checked="" type="checkbox"/> | <input type="checkbox"/> Clinical data |
| <input checked="" type="checkbox"/> | <input type="checkbox"/> Dual use research of concern |

- | n/a | Involvement in the study |
|-------------------------------------|---|
| <input checked="" type="checkbox"/> | <input type="checkbox"/> ChIP-seq |
| <input checked="" type="checkbox"/> | <input type="checkbox"/> Flow cytometry |
| <input checked="" type="checkbox"/> | <input type="checkbox"/> MRI-based neuroimaging |